SiD Letter of Intent

Vertex and Tracking Companion Document

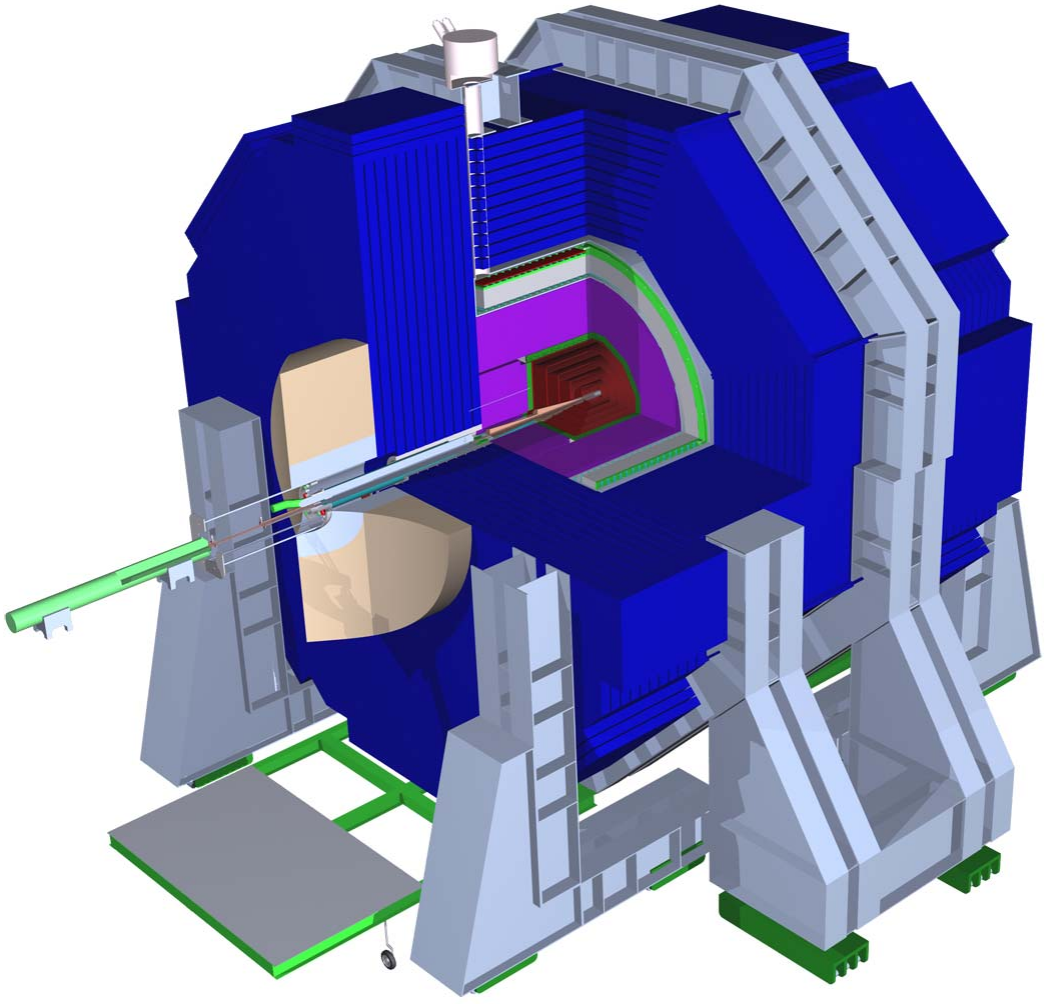

Contents

1.1 Vertex and Tracking System

1.1.1 Introduction

The tracking system of the SiD detector uses a barrel-disk layout. Five cylindrical layers of pixel detectors surround the interaction point, complemented by four disks of pixel sensors on either end. These inner layers are followed by a set of five barrels of silicon strip sensors in the central region, capped by four nested disks of silicon strip sensors at both ends. To provide uniform hit coverage, three disks with pixel sensors are provided in the transition region between the inner and outer disks in both the forward and backward region.

Within the SiD detector concept the tracking system is regarded as an integrated tracking system. Although individual detector components can be identified in the vertexing and tracking system, the overall design is driven by the combined performance of the pixel detector at small radius, the outer strip detector at large radius and the electromagnetic calorimeter for the identification of minimum ionizing track stubs. The physics at the ILC requires good track reconstruction and particle identification for a wide array of topologies. The main elements for the pattern recognition are the highly pixellated vertex detector and the low occupancy outer strip detector.

Early track finding studies relied on identifying tracks in the vertex detector, where pattern recognition is simplified by the fact that precise three-dimensional information is available for each hit. Tracks found in the vertex detector are then propagated into the outer tracker, picking up additional hits. While good performance was achieved using this approach, an important class of events, notably highly boosted b-quarks, will decay at radii that do not allow for pattern recognition in the vertex detector alone. To provide additional flexibility, a more general tracking algorithm has been developed that can seed tracks using any three layers in the tracker, either from the outer tracker, the vertex detector or a combination of both. Tracks produced by the decay products of long-lived particles, however, can leave too few hits in the tracker to be reconstructed using only hits in the tracking volume. Obvious examples are long-lived particles such as K_s^0's and Λ's. The detector should also be capable of detecting new physics signatures that would include long-lived exotic particles like those predicted by some gauge-mediated supersymmetry breaking scenarios. There are also issues of reconstructing kinked tracks produced by particles that lose a substantial portion of their energy in the tracker, as well as reconstructing backscatters from the calorimeter. To capture the tracks from these event topologies a calorimeter-assisted tracking algorithm has been employed. This algorithm uses the electromagnetic calorimeter to provide seeds for pattern recognition in the tracker. The very fine segmentation of the EM calorimeter allows for detection of traces left by minimum ionizing particles. These can be used to determine the track entry point, direction, and sometimes curvature with a precision sufficient for extrapolating the track back into the tracker. This set of complementary algorithms provides for very robust pattern recognition and track finding and it is the performance of this integrated tracking system that determines the overall physics reach of the detector.

In the next section the boundary conditions for operating an integrated tracking system at the ILC will be presented. These will form the basis for the choice of design of the overall system, which will be discussed in the following section. The remainder will describe the

details of the design, the implementation of the detector in the Monte Carlo simulations and some preliminary results. We will conclude with a discussion of the R&D needed in the next few years.

1.1.2 Beam Environment

The bunch structure of the ILC, which consists of trains of 2820 bunches which are spaced 308 ns apart, repeated 5 times per second, and the physics and machine backgrounds resulting from bunch-bunch collisions, impose many constraints on ILC detector technologies and on the readout electronics. The two main backgrounds are backgrounds from the interaction point and machine backgrounds. Events contributing to the first category are

- disrupted primary beam
- beamstrahlung photons
- e^+e^--pairs from beam-beam interactions
- radiative Bhabha events
- hadrons or muons from $\gamma\gamma$ interactions.

The second category is populated with events from

- direct beam losses
- beam-gas interactions
- collimator edge scattering
- synchrotron radiation
- neutron back-shine from the beam dump
- extraction line losses

Although these constraints are mild compared to those imposed on LHC detectors, the high flux of photons concomitant with the collisions, from virtual sources and beamstrahlung, results in the copious production of e^+e^--pairs as well as the frequent production of muon pairs and hadronic interactions. The e^+e^--pairs account for most of the background in the inner detectors, directly as charged tracks with low transverse momentum. They also cause a general flux of photons in the MeV energy range, which results when they shower in the beam calorimeters on the front face of the final quadrupoles. These photons, and the higher transverse momentum muons and charged and neutral hadrons which also result from photon-photon interactions, spray the entire detector with charged particles and photons.

As will be quantified in the following sections, SiD is largely immune to these backgrounds because the detector as a whole is only sensitive to backgrounds associated with a

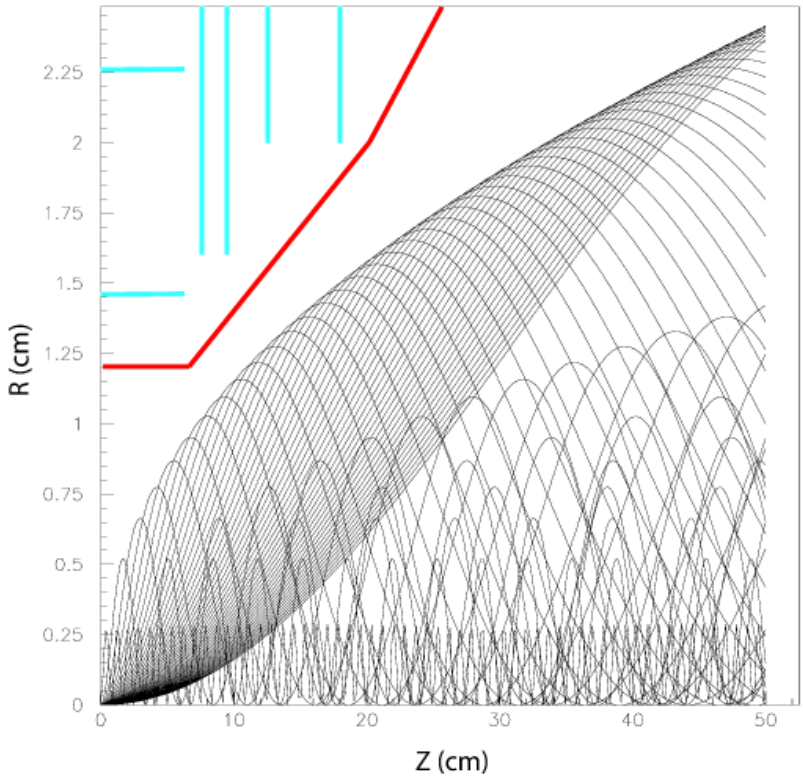

Figure 1.1: Maximum envelope of the e^+e^--pair backgrounds in a 5 Tesla field. Indicated is the 12 mm radius beampine.

single bunch crossing. The pixel detector is assumed to have a bunch-by-bunch timestamp and a channel-by-channel buffer, which is 4 deep in the current design, will store hits over the course of the entire bunch train and record each responsible bunch crossing, for the silicon strip detector. Similarly for the electromagnetic calorimeter. Consequently, SiD is sensitive only to the physics and backgrounds of a single bunch crossing.

The effects of these backgrounds have been evaluated with the Guinea-Pig program. The nominal ILC beam parameters have been used for the simulation. The beamline magnets up to about 20 m from the interaction point have been included, using a beam crossing angle of 14 *mrad*. The nearest quadrupole magnet of the final doublet ends at 3.51 m. The detector solenoid field is 5 Tesla, and a field map instead of a constant field is used for the calculations of the beam backgrounds. The beam pipe through the central portion of the vertex detector has been taken to be all-beryllium. Within the barrel region of the vertex detector, the beryllium beam pipe has been taken to be a straight cylinder with inner radius of 1.2 cm and a wall thickness of 0.04 cm. At $z = \pm 6.25$ cm, a transition is made to a conical beam pipe with a wall thickness of 0.07 cm. The half angle of the cone is 3.266^o. Transitions from beryllium to stainless steel are made beyond the tracking volume, at approximately $z = \pm 20.5$ cm. The initial stainless steel wall thickness is 0.107 cm; it increases to 0.15 cm at approximately $z = \pm 120$ cm. The half angle of the stainless steel cone is 5.329^o. The

inner profile of the beam pipe is dictated by the need to avoid the envelope of beam related backgrounds, as shown in Fig. 1.1. A titanium liner of thickness 0.0025 cm is has been included within the central beryllium portions of the beam pipe. The liner provides shielding against soft X-rays (¡ 10 keV). The titanium liner in the cone section of the beam pipe is expected to be a factor of 3 thicker than in the central region to take into account the incidence angle of back-scattered photons.

With these assumptions, the background in the tracking detector has been evaluated. The background hits in the vertex detector come predominantly from the e^+e^-pairs. The number of VXD hits in the first barrel layer of the vertex detector is expected to be nearly 80 hits/mm^2/train over the full train for 500 GeV operations; at 1 TeV, in the high luminosity option, this number rises to about 400 hits/mm^2/train.The charged backgrounds are appreciable only at the very small radii affecting the vertex detector and inner most sections of the forward tracking system. The hit densities from pairs in the forward vertex disks at their innermost radii match the densities in the barrel section of the detector, and the densities fall off with increasing radius. So the limits determined for the barrel detector should apply also to the forward disks. These boundary conditions, imposed by the machine, have led to the design described in the following section.

1.1.3 Vertex Detector Design

The vertex detector integrates with the outer tracker and remainder of the detector to provide significantly extended physics reach through superb vertex reconstruction – primary, secondary and tertiary. To date, all vertex detectors at collider experiments are silicon based, and the vertex detector for the SiD concept is no exception. The vertex detector consists of a central barrel section with five silicon pixel layers and forward and backward disk regions, each with four silicon pixel disks. Three silicon pixel disks at larger $\mid z \mid$ provide uniform coverage for the transition region between the vertex detector and the outer tracker. Barrel layers and disks are arranged to provide good hermeticity for $\cos\vartheta \leq 0.984$ and to guarantee good pattern recognition capability for charged tracking and excellent impact parameter resolution over the whole solid angle. A side-view of the vertex detector is shown in Fig. 1.2. For clarity, the silicon support structures have not been drawn in the right hand side of this figure.

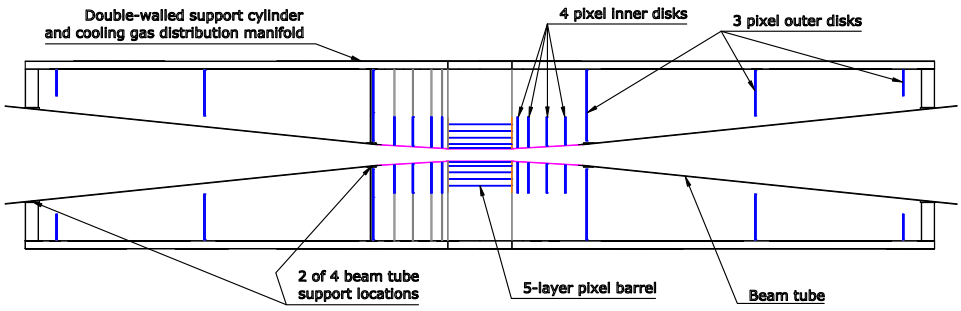

Figure 1.2: R-z view of the vertex detector. The right hand side has been drawn without the support structures.

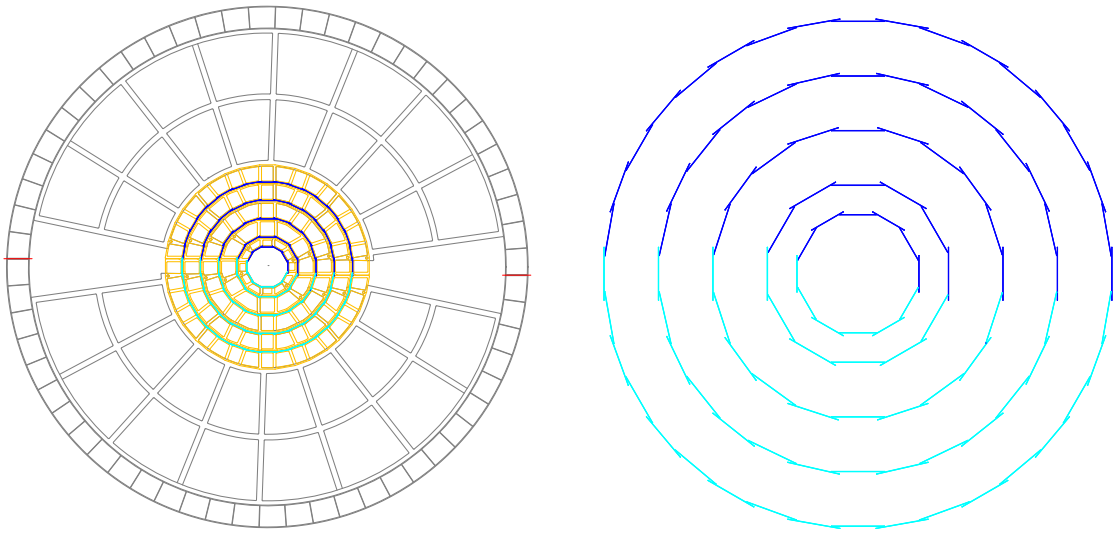

Figure 1.3: Barrel end view of the vertex detector (left) and layer arrangement of the silicon sensors only (right).

Vertex detectors are generally plagued by a mismatch in thermal expansion coefficients between the silicon and its support structures. Moreover, these supports in general add to the material budget in a region of physics phase space where it is least desired. To partially address those considerations, an 'all-silicon' structure is proposed for the vertex detector barrel. In this context, 'all-silicon' means that sensors of each barrel layer are joined along their edges with adhesive to approximate an arc of a circular cylinder, and no other structural materials are present in that limited region. Thermal distortions are reduced by limiting material to that of the sensors themselves and adhesive, which has a low elastic modulus relative to silicon. Longitudinal deflection of a layer is controlled by the cylindrical shape, thereby minimizing additional material. The quasi-cylindrical shape of a layer is maintained by annular, flat rings at each end. In turn, the end rings are joined to one another and connected to an outer support cylinder via web-like support disks. Though various possibilities are still under consideration for the end ring and support disk material, we would like a material, such as carbon fiber laminate or silicon-based foam, which has a longer radiation length than that of silicon. Because other materials than silicon are used for external mechanical connections, the term "all-silicon" is placed in quotes.

At this time, many sensor options remain under investigation and we have yet to choose a specific sensor technology. The candidates for sensor technology are discussed in the R&D section. The design presented here makes the assumption, independent of sensor technology, that fabrication and assembly of the detector occur at room temperature and that the sensors are operated at a temperature $>$ -10 ^{0}C. Because sensors are used as a structural element and other material has been minimized, our design favors relatively thick sensors. The sensor thickness has been taken to be 75 μm. Sensor cut width is 8.68 mm in the innermost layer and 12.58 mm in all other layers. The cut sensor length for all layers is 125 mm.

To allow assembly about the beam pipe and later servicing, all barrels, disks, and

support elements of the vertex detector are split about approximately the horizontal plane into top and bottom sub-assemblies. Once mated, the two sub-assemblies are supported from the beam pipe and stiffen the portion of the beam pipe passing through them. Fig. 1.3 is an end view of the barrel region, showing the five silicon barrel layers and their spoked support disk. The outer rings indicate the double-walled carbon fiber support tube. Since the silicon is very thin on the scale of this drawing, the layer arrangement of the individual sensors is shown in the right drawing in Fig. 1.3 for clarity.

The five layers are arranged at radii ranging from 14 to 60 mm. The vertex detector also has four disk layer sensors which are attached to carbon fiber support disks at z positions ranging from about 72 to 172 mm. The innermost disk covers radii from 14 mm out to 71 mm; the outermost, from 20 mm to 71 mm. Forward tracking continues beyond the vertex detector proper with three additional small pixel disks, extending in z from about 207 to 834 mm. Their inner radii range from 29 to about 117 mm, and their outer radius is about 166 mm.

The beam pipe through the central portion of the vertex detector has been taken to be all-beryllium. Within the barrel region of the vertex detector, the beryllium beam pipe has been taken to be a straight cylinder with inner radius of 1.2 cm and a wall thickness of 0.04 cm. At $z = \pm 6.25$ cm, a transition is made to a conical beam pipe with a wall thickness of 0.07 cm. The half angle of the cone is 3.266^o. Transitions from beryllium to stainless steel are made beyond the tracking volume, at approximately $z = \pm 20.5$ cm. The initial stainless steel wall thickness is 0.107 cm; it increases to 0.15 cm at approximately $z = \pm 120$ cm. The half angle of the stainless steel cone is 5.329°. The inner profile of the beam pipe is dictated by the need to avoid the envelope of beam-strahlung produced e^+e^--pairs.

To prevent bending of the small-radius portion of the beam pipe and ensure good stability of vertex detector position, the outer vertex detector support cylinder is coupled to the beam pipe at four longitudinal locations: $\pm$ 21.4 and $\pm$ 88.2 cm. Inner and outer support cylinder walls are 0.26 mm thick. They are made from four plies of high modulus carbon fiber, resin pre-preg. Wall separation is 15 mm. We propose to deliver cooling air via the vertex detector outer support cylinder. To allow that, the two walls of the cylinder would be separated by radially-oriented ribs running the full cylinder length. Calculations assumed ribs at 60 azimuths. Openings, each approximately 12.2 mm x 15 mm, at 18 z-locations in the inner cylinder wall distribute flow to the various disk locations and to the barrel.

For our initial investigation the flow for barrel cooling was assumed to be from one barrel end to the other. The average power dissipated in a sensor was taken to be 131 μW/mm^2. That corresponds to a total power of about 20 Watts for the 5-layer barrel considered. These numbers presume power cycling, i.e., that most power is dissipated during the roughly 1 ms during which the beam train is present, and that power is turned off in the 199 ms between trains. We assumed that power is distributed uniformly over the sensor active surface and that both sensor surfaces participate in heat removal. Supply air temperature was taken to be -15 ^{0}C. For a given sensor, power transferred inward through the carbon fiber cylinder was taken to be proportional to the surface contact between the sensor and carbon fiber. Thermal impedance through silicon, epoxy, and carbon fiber laminate has been included, but turns out not to be particularly significant. The remaining power was assumed to be transferred outward into the layer to layer gap. For flow and heat transfer calculations, the gap between

barrel layers was taken to be 1 mm less than the nominal layer spacing. Laminar flow was assumed.

The cooling power was evaluated as a function of Reynold's number, which was required to be the same for all barrel gaps. To provide laminar flow and limit the likelihood of vibration, a maximum Reynold's number of 1800 was considered. Cooling with turbulent flow and acceptable stability of sensor positions may also be possible, but remains to be investigated.

As mentioned before, openings, each approximately 12.2 mm x 15 mm, are envisioned at 18 z-locations and 60 azimuths in the inner cylinder wall to distribute flow to the various disk locations and to the barrel. At each azimuth, the cell through which flow passes was approximated by a rectangle of height 15 mm and width 18.246 mm. The wall thickness was assumed to be 0.26 mm for both cylinders and for all ribs. The result was a Reynold's number of 3105 in the portion of the cell which sees full flow, which indicates flow will be turbulent. Since a portion of the flow exits the cell at each opening, the Reynold's number drops to 1725 at approximately z = 51.9 cm (a short distance inboard of the two outermost disks). While entrance effects may remain, flow should gradually become laminar after that point. Supply and return connections to the outside world remain to be fully evaluated.

The sensors of the outermost layer, where it is easier to provide cross-section for air flow, and sensors in the innermost layer, where we have assumed that the beam pipe includes thermal intercepts and will introduce no heat, are noticeably cooler than sensors of the three middle layers, rather independent of the flow. In the outermost layer, the cross section provided for air flow could be reduced to raise the temperature of that layer. In the gap between the innermost layer and the beam tube, flow is likely to be lower and temperature higher, once supply and return distribution patterns of air flow have been taken into account. Higher flow rate clearly improves the uniformity of sensor temperatures end to end and reduces the difference between the temperature of a sensor and the cooling air. All flow rates which have been considered, lead to temperature variations which should be acceptable for dimensional stability, which is crucial for high precision vertexing. The time-dependent effects of power cycling remain to be investigated. Those depend on the thermal mass presented by the barrels and the details of the way in which power is cycled. External heat input to the barrel has been assumed to be negligible. Satisfying that assumption will require reasonable care in designing cables, in providing heat intercepts should they be needed, and in providing an external thermal enclosure. The outer support cylinder of the vertex detector offers a natural thermal enclosure. Details of end openings in barrel membranes remain to be included. Those openings provide a natural mechanism for adjusting relative flow between barrel layers. A membrane between the outermost barrel layer and the vertex chamber support cylinder would ensure that flow does not excessively bypass the barrel-to-barrel gaps.

Similar calculations have been made to understand disk cooling. Those calculations are based upon barrel results with a Reynold's number of 1800 (barrel flow = 20 g/s). Disk power dissipation is dependent upon the sensor technology chosen, and that choice remains to be made. At each end of the barrel region, the first four disks have been assumed to employ pixel sensors. For heat removal calculations, they have been assumed to dissipate the same power per unit area as the pixel sensors of the barrels. The result is a total power of 16.9

Watts for all eight disks and an air flow of 16.4 g/s.

For the next three disks outboard at each end the sensors were treated as silicon pixels with $\frac{1}{4}$ the power dissipation per unit area as that of barrel pixels; that assumes pixels which are twice as large. The result was a total power of 13.25 Watts for all six disks and an air flow of 12.8 g/s. The total required flow is the sum of that for the barrel, inner disks and outer disks, that is, 48.65 g/s. To take into account warming of air and to allow a small margin, flow calculations assumed an air temperature of -20 ^{0}C and a flow rate of 50 g/s.

The readout scheme for the SiD vertex detector is closely coupled to the sensor technology. Any technology will be required to adequately address hit occupancies, so that pattern recognition is not overwhelmed by background. Ideally the readout will associate hits with single beam crossings. The column-parallel CCD, DEPFET, and many MAPs-based readout schemes utilize a rolling shutter during the bunch train. In this scheme the detector frame is completely read out multiple times during the bunch train, with the effective time resolution equivalent to the frame readout time. The ISIS technology and some MAPS-based designs use in-pixel storage of multiple analog samples, with full readout between trains. The Chronopixel design stores analog pulse heights and digital and/or analog time stamps in the pixel, also with readout between trains.

The vertex detector readout is illustrated using the scheme with in-pixel storage of analog information and digital time stamps used in the 3D-VIP chip. In this scheme analog and digital information is stored within a pixel during the bunch train and read out between trains. Pixel complexity is minimized by storing address information on the periphery of the chip. Table 1.1 summarizes the power consumption of this readout scheme. Electrical connections of about one meter from the ladders to optical links installed on the support tube have been assumed. Assuming 32 bits are used per hit and 100 pF interconnect capacitance at 1.5 V, the local readout consumes 0.24 Watts of average power. If each of the 108 ladders is independently driven with a 200 MHz clock speed, the inner layers would dominate the readout time at 75 ms/ladder. The peak power at the start of readout, with all layers reading at 200 MHz, is 4.8 Watts. This could be reduced to 1.3 Watts if the outer layers are clocked more slowly to match the 75 ms inner layer readout time, or to a value close to the average power if the clock rate on each layer is tuned to match the data load. The bit rate from the entire vertex detector is about 2 Gbits/sec.

Layer	Number of ladders	hits/crossing	hits/train	bits/train	Readout time (ms)
Layer 1	12	2000	$5.6\ 10^6$	$1.8\ 10^8$	75
Layer 2	12	1200	$3.4\ 10^6$	$1.1\ 10^8$	45
Layer 3	20	800	$2.3\ 10^6$	$7.2\ 10^7$	18
Layer 4	28	450	$1.3\ 10^6$	$4.1\ 10^7$	7.3
Layer 5	36	400	$1.1\ 10^6$	$3.6\ 10^7$	5.0

Table 1.1: Readout rates for the vertex detector assuming 3D-VIP readout scheme.

The power delivery is expected to be a major source of material contribution. The

instantaneous power of many of the sensor technologies could be 50W or more per sensor. One naïve scheme is to deliver power through short copper wires with e.g. 300μm diameter or flat cables to each sensor and use DC-DC conversion on the vertex detector support cylinder from a higher supply voltage. A low mass local DC-DC conversion near the sensors with higher incoming voltage would be more favorable in many respects if it can be realized. An extension of the radiation hard optical transmission technology used for LHC detectors could be foreseen as the means of control and data transmission. The material from the thin fibers is expected to be significantly less than the material involved in power delivery. However, the major issue for both power delivery and signal transmission is the connection to the thin sensors. The miniaturization of the connectors and the transceivers will be key R&D projects to ensure the material minimization. For simulation purposes the readout section at each end of a sensor is assumed to be a 2mm tall and 5mm long block spanning the full width of the sensors with same radiation length as G10. The number of radiation lengths represented by vertex detector structures, averaged over φ in most cases, is given in Fig. 1.5.

In a 5 T solenoidal field, forces and torques acting on radial runs of power delivery cabling can be significant. When coupling with the cyclic delivery of power, as we have assumed to allow gas cooling, the result can be vibrations which are transmitted from the cables into sensors and their support structures. To mitigate those possibilities, we propose to deliver power on flat-lines with three conductor layers. The central layer, for example, would serve to supply power and the two outer layers would serve as power returns. To avoid ground currents and ensure that supply and return currents balance within a cable, some combination of isolation of power sources and isolation of sensor grounds is envisioned. Then, provided the two return currents of a cable are equal, net force and torque on the cable due to interaction of currents with the magnetic field would be zero. Power/ground isolation would also eliminate issues that arise when portions of the vertex detector are unpowered while other portions are powered. We note that the total conductor in a cable can be the same as in a more traditional, two-conductor-layer cable. We also note that coaxial cables could be used instead of flat-lines.

Power distribution at sensor locations should also be scrutinized. In the barrel, radial current runs within sensors are relatively short, thereby limiting forces and torques associated with the magnetic field. In the disks, care will need to be taken to avoid supply/return current loops within sensors. In both locations, limitation of support structure material lessens the ability of those structures to resist unexpected forces and torques. Careful design and testing will be necessary.

During silicon servicing, the vertex detector and beam pipe remain fixed while the outer silicon tracker rolls longitudinally (see Fig. 1.4). To allow that motion, to enable placement of the outer silicon tracker elements at the smallest possible radius, and to leave space for any additional thermal insulation which might be needed, the outer radius of the vertex detector, including its support structures, has been limited to 18.5 cm. To maximize physics potential, the inner radius of vertex detector elements has been chosen to be as small as practical consistent with beam-related backgrounds and the beam pipe profile. In the barrel region, the minimum radius to a sensor surface is 1.4 cm, governed by the beam backgrounds as discussed earlier.

The number of radiation lengths represented by vertex detector structures, averaged

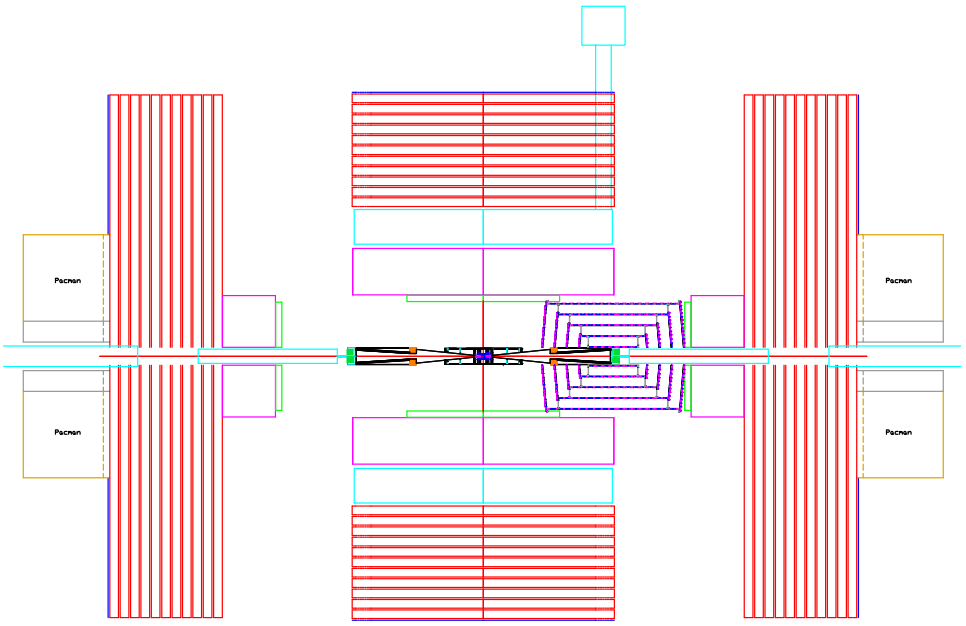

Figure 1.4: Tracker in the open position for servicing of the vertex detector.

over φ in most cases, and the vertex detector hit pattern are shown in Fig. 1.5. Shown are the contributions of the individual subdetectors to the total number of hits on a particle track with infinite momentum. The irregular features correspond to the transition regions. Overall there are more than five pixel hits on a particle trajectory down to angles of about 10°.

The irregular features of the readout and service contributions to the material budget are due to discrete elements at the end of the sensors. Most of the readout material is beyond the first few layers of the vertex detector, so that their influence on the impact parameter resolution is limited. The fact that the amount of material in these elements is comparable to that of the sensors or mechanical supports calls for close attention to the design of low mass power delivery and signal transmission components. If the readout and service material can indeed meet what is in the current model, the material balance would be more favorable for a considerable portion of the endcap region compared to the $1/\sin\vartheta$ growth for a long barrel geometry. With this material balance, the benefit of the endcap geometry in spatial resolution with a better track entrance angle and smaller radial alignment effect, is a meaningful advantage. Table 1.2 summarizes the main parameters of the vertex detector.

1.1.4 Tracker Design

The ILC experiments demand tracking systems unlike any previously envisioned. In addition to efficient and robust track-finding, the momentum resolution required to enable precision physics at ILC energies must improve significantly upon that of previous trackers. The design must minimize material in front of the calorimeter that might endanger particle-flow jet reconstruction. Even with the largest feasible magnetic field, the tracking volume is quite large so that tracker components must be relatively inexpensive and easily mass-

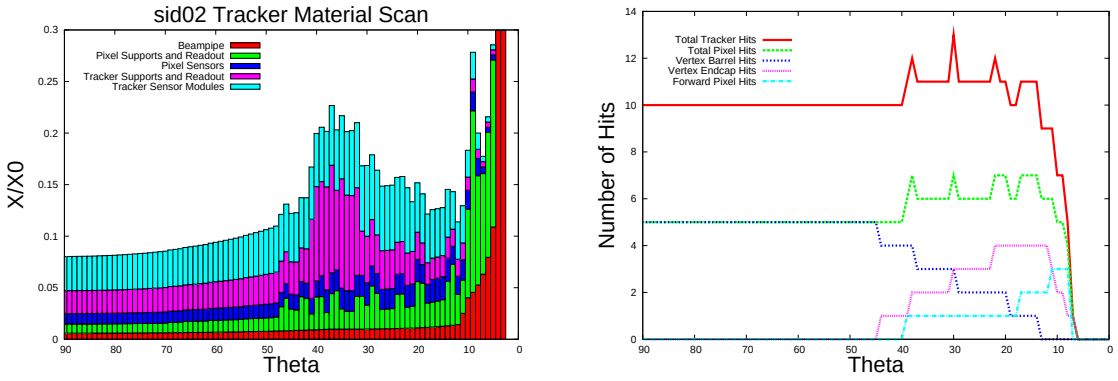

Figure 1.5: Material budget of the tracking system (left) and number of hit layers in the tracking system as a function of polar angle (right).

produced. Finally, the tracker must be robust against beam-related accidents and aging. These requirements have led to the choice of silicon microstrip detectors for the tracker. The outer silicon tracker design consists of five nested barrels in the central region and four cones in each of the end regions. The support material of disks follows a conical surface with an angle of 5-degrees with respect to the normal to the beamline. Sensors on disk modules are normal to the beam line. The barrel supports are continuous cylinders formed from a sandwich of pre-impregnated carbon fiber composite around a Rohacell core. The support cones are also double-walled carbon fiber structures around a Rohacell core. Each support cone is supported off a barrel. Spoked annular rings support the ends of each barrel cylinder from the inner surface of the next barrel out. It is expected that openings will be cut in the support structures to reduce material, once module mounting locations are known. These openings not only reduce the number of radiation lengths, but also reduce the weight to be supported. Openings may also be needed for an optical alignment system. It is envisioned that the electronics and power cables that supply entire segments of the detector are mounted on these spoked rings. The dimensions of the barrels and cones are given in Table 1.3. Fig. 1.6 shows an elevation view of the tracking system.

Because of the very low occupancies in the outer barrel, the nominal design for the outer tracker employs only axial readout in the barrel region. In the baseline design, the barrels are covered with silicon modules. Modules are comprised of a carbon fiber composite frame with rohacell/epoxy cross bracing and have one single-sided silicon sensor bonded to the outer surface. Sensors are obtained from one single 6-inch wafer and are approximately 10 cm $\times$ 10 cm. This size sets the longitudinal readout segmentation of the barrel detectors. The sensors are 300μm thick with a readout pitch of 50 μm and intermediate strips. Full coverage is obtained by ensuring small overlap both longitudinally and azimuthally. Azimuthal overlap is obtained by slightly tilting the sensors. The angle by which the sensor is tilted partially compensates for the Lorentz angle of the collected charge in the 5T field of the solenoid. Longitudinal overlap is obtained by placing alternate sensors at slightly different radii. Fig. 1.7 shows a detail of the overlap in the z and Rφ direction, respectively.

Modules are attached to the cylinder using a PEEK (Poly-Ether-Ether-Ketone) mounting clip. The readout chips and cables are mounted directly to the outer surface of the silicon

Barrel Region	R (mm)	Length (mm)	Number of sensors in φ
Layer 1	14	125	12
Layer 2	21	125	12
Layer 3	34	125	20
Layer 4	47	125	28
Layer 5	60	125	36
Disk	R_{inner}	R_{outer}	z_{center}
Disk 1	15	75	76
Disk 2	16	75	95
Disk 3	18	75	125
Disk 4	21	75	180
Forward Disk	R_{inner}	R_{outer}	z_{center}
Disk 1	28	166	211
Disk 2	76	166	543
Disk 3	118	166	834

Table 1.2: Parameters of the vertex detector. Units are mm.

sensors. The cables supply power and control to the readout chip from electronics located at the ends of the barrel.

Fig. 1.8 shows an Rφ-view of the barrel region. The outermost disk is projected onto the barrel layout in this figure. For pattern recognition in the disks, small angle stereo will provide 3d-space points. The current design has two single-sided wedge detectors back-to-back, with strips at $\pm 6^\circ$ with respect to the long axis of the wedge for a stereo angle of 12°. Please note that in Fig. 1.5 the hits from a pair of sensors, corresponding to one 3d-space point, is represented as one hit. Two types of sensors are needed to tile the disks, one type at the inner radii and a second sensor type to populate the area at the outer radii. Also in the forward region sensors will be 300μm thick with intermediate strips. The conical support disk design ("lampshade design") provides an elegant way to implement module overlaps, eliminating any dead areas, and allows for easy module mounting and cable routing. Fig. 1.9 shows a side view of modules mounted on a disk. The support disks have penetrations for cable routing. In this scheme all cable are routed on the inner surface of the disks.

The inner radius of the outer tracker is set by forward, beam-monitoring calorimetry and beamline elements, over which the tracker is intended to slide. Once the tracker inner radius is set, the outer radius of vertex detector structures follows. During servicing, the vertex detector and beam pipe remain fixed while the outer silicon tracker rolls longitudinally, as shown in Figure 1.4. To allow that motion, no element from the outer tracker can be at a radius smaller than the radius of the vertex detector outer support cylinder. To allow for good acceptance and pattern recognition, the small angle region is covered by three small

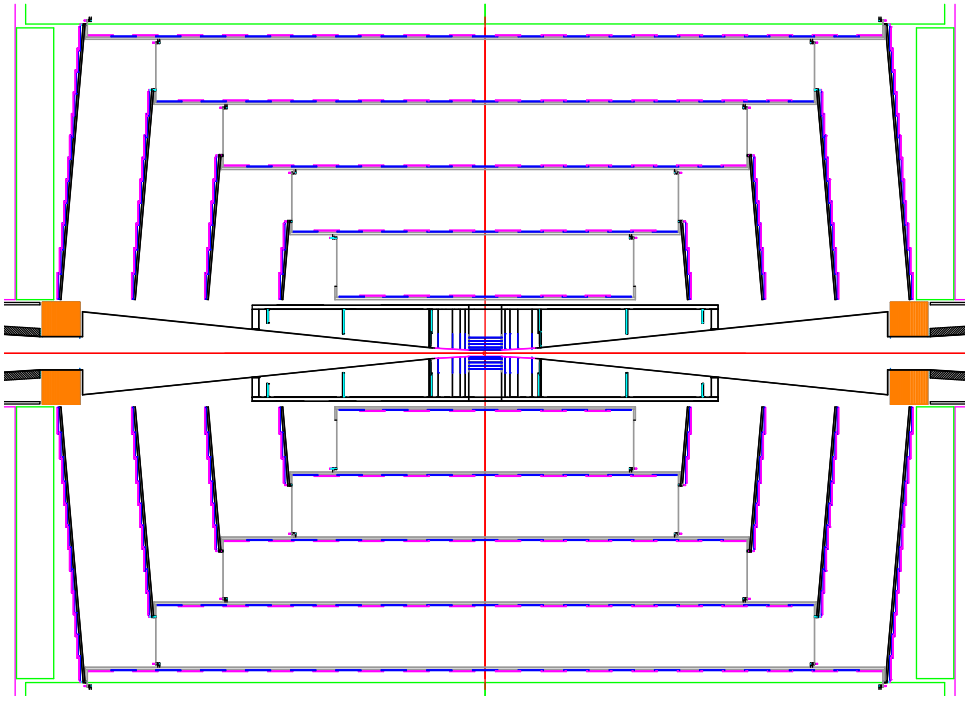

Figure 1.6: R-z view of the whole tracking system.

silicon disks at each end with radius below 20 cm, which has been described in the section on the mechanical layout of the vertex detector. Figure 1.5 shows the cumulative amount of material as a function of polar angle as modeled in the Monte Carlo. The lowest curve shows the contribution from the beampipe followed by the contribution of the support and readout structures for the pixel detector. The material corresponding to the various readout elements has conservatively been assumed to be uniformly distributed in the tracker volume. The next curve indicates the material due to the active vertex detector elements. The outer two curves give the amount of material of the tracker supports and readouts and the silicon modules, respectively. It should be noted that the material corresponding to the silicon modules includes the module supports in addition to the silicon.

Overall a material budget of about 0.8% X_0 per layer is achieved for the outer tracker. Table 1.3 lists some of the parameters of the tracker for the current design. There are 8130 modules in the barrel region and 2848 modules for the end regions combined.

1.1.5 Tracker Module Design

To build a large volume silicon tracker within an acceptable material budget is quite challenging. The scale of the project puts a premium on minimizing the number of different components and achieving a modular construction process, while at the same time limiting the mass budget of the overall system. To achieve this goal, the design of the SiD tracker employs silicon modules with novel characteristics.

A module is the most elementary working component of the SiD tracker. Each barrel

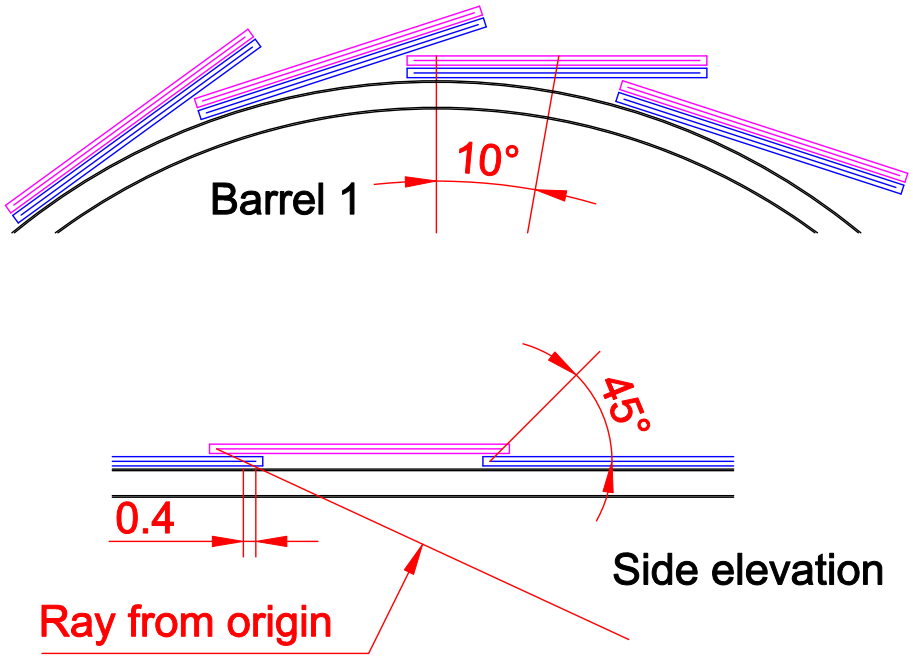

Figure 1.7: Detail of the sensor overlap in the barrel region in the z and Rφ projection.

module has a single square sensor, while an endcap module consists of two wedge-shaped sensors placed back-to-back to create a stereo pair. Each sensor is read out by a pair of 1024-channel readout ASICs, called KPiX. A short Kapton readout cable provides power and control signals to the KPiX chips and carries digitized signals to the edge of the module where they are transmitted to a longer bus cable which transmits them to the end of the tracker. There is neither a hybrid circuit board nor a mechanical cooling path since gas flow can provide the required cooling.

The barrel sensors for the SiD tracker are square, 9.53 cm on a side, 300 μm thick, <100>, single-sided, double-metal, p^+-on-n sensors with 25 μm sense pitch and 50 μm readout pitch. This floating-strip design provides the best possible single-hit resolution for a reasonable channel count as long as the signal-to-noise ration remains large, motivating the use of short readout strips to reduce capacitance. The sensors are AC-coupled with polysilicon bias resistors. Aside from having a different shape, the wedge sensors in the endcap are essentially the same. Fig. 1.10 shows a picture of a prototype sensor. Initial tests of several SiD prototype sensors indicate that the fabrication was successful. By measuring the resistance of the strips from end-to-end, as well as the resistance from one end of the strip to the end of the corresponding readout trace, the separate strip and trace resistances can be estimated. This was done for two sensors, and the strip resistance was found to be approximately 550 Ω. The resistance of a typical readout trace was found to be approximately 200 Ω. Measurements of the CV characteristics suggested a depletion voltage of approximately 50 V; a typical CV curve is shown in Fig. 1.11. At full depletion, a typical leakage current (all channels combined) was 300 nA, or about 160 pA per channel for the 1840-channel sensor.

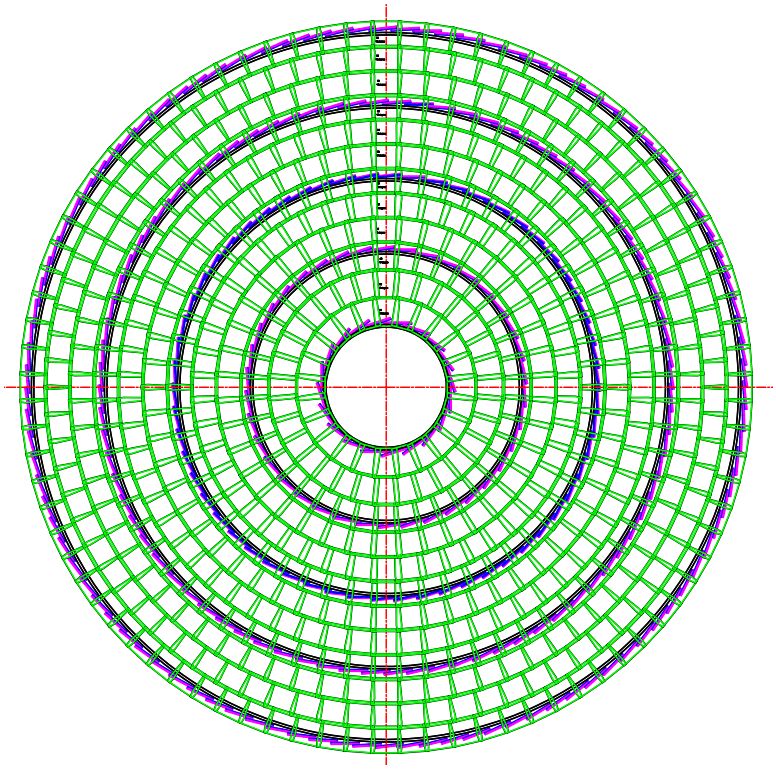

Figure 1.8: Rφ projection view of the tracker barrels and disks.

The pair of KPiX readout chips are bump-bonded directly to the face of the sensor and the readout strips of the sensor connect to the bonding array via double-metal traces (see Figure 6). Fig. 1.12 shows a detail of the double-metal routing of the traces for one half of the sensor to one of the two readout chips. The pads for bump-bonding to the readout chip are 70×70 μm^2, with a 200 by 500 μm pitch. A necessary consequence of this scheme is that the power, control and readout signals of the KPiX chip must also be routed to a bonding array from the readout cable on the double-metal layer, also shown in Fig. 1.12. Extensive modeling of the capacitances and the behavior of the KPiX chip has refined the sensor design with an emphasis on low-impedance power delivery, minimal readout capacitance and reduced coupling to potential noise sources on the power and readout traces. A reduced set of specifications for prototype barrel sensors is given Table 1.4.

The central component of the readout architecture proposed for the SiD tracker is the 1024-channel KPiX readout chip. The KPiX chip is designed for pulsed power, minimizing the input current between bunch trains. This reduces the power consumption to 20 mW on average for a 1024-channel KPiX chip, or 40 mW for a single-sided module allowing for gas cooling of the tracker. The chip has four time-stamped analog buffers per channel that store signals from the detector until the inter-train period for digitization and readout. As a result, the only digital activities on KPiX during the bunch train are a synchronous LVDS clock and individual comparators firing when a channel crosses the readout thresholds. This low-noise mode of operation during the bunch train allows KPiX to be mounted directly to the sensor without inducing large RF pickup on the strips.

Figure 1.9: Detail of the sensor overlap and cable routing for the tracker disks.

A low mass readout cable, called a "pigtail", is glued to the module and wirebonded to the double metal power and readout traces. The other end of the pigtail connects the module to a two-meter long extension cable which connects, in turn, to power and data concentrator boards at the end of the barrels, each of which serves approximately 20 sensors. The cable includes two pairs of traces each for analog and digital power, sixteen traces (eight per KPiX readout chip) for digital control and readout, along with one pair for sensor bias. The pigtail cable has a pair of tabs near the sensor edge for connection of the sensor bias as well as surface mount pads for bias and power filtering, and for LVDS signal termination resistors.

These single-sensor sized modules require minimal support, only enough to hold the sensors flat and provide stable and repeatable mounting. The support frame of a module is composed of a pair of thin, high-modulus carbon-fiber skins sandwiched around a Rohacell core. The frame has injection-molded carbon fiber filled PEEK strips on two edges into which precision silicon-nitride balls are molded, providing a kinematic, three-point mount. Mounting clips are used to place the module on the support structure. They are also injection-molded carbon fiber filled PEEK and include custom silicon nitride mating parts for the mounting balls of the support frame. The current barrel module design represents roughly 0.5% X_0 per unit coverage including the mounting clips and longer readout cables needed to connect the pigtails to the power and readout distribution boards mounted on the support rings at the ends of the barrels. Fig. 1.13 shows a sketch of a prototype barrel module.

Although a detailed design for the forward modules awaits further simulation study, it is presumed that these modules will be of similar design. The detector model currently being simulated for performance studies has modules utilizing two different wedge-shaped sensor designs for the endcaps, as shown in Fig. 1.14.

An alternative approach to the KPIX front-end readout ASIC, the Long-Shaping-Time Front End (LSTFE) ASIC, has also been under development. The LSTFE ASIC features a long (~ 1.5 μs) shaping time, typical for ILC silicon sensor readout applications, that limits

Barrel Region	$\langle R \rangle$ (cm)	Length of sensor coverage (cm)	Number of modules in φ	Number of modules in z
Barrel 1	21.95	111.6	20	13
Barrel 2	46.95	147.3	38	17
Barrel 3	71.95	200.1	58	23
Barrel 4	96.95	251.8	80	29
Barrel 5	121.95	304.5	102	35
Disk Region	z_{inner} (cm)	R_{inner} (cm)	R_{outer} (cm)	Number of modules per end
Disk 1	78.89	20.89	49.80	96
Disk 2	107.50	20.89	75.14	238
Disk 3	135.55	20.89	100.31	428
Disk 4	164.09	20.89	125.36	662

Table 1.3: Parameters of the tracking detector.

readout noise from capacitive and series-resistance load. After amplification and shaping, the signals are split in two and directed to two separate comparators. One runs at a high ($\sim$ 1.2 fC) threshold to suppress noise, while the other runs at a low ($\sim$ 0.4 fC) threshold to maximize the information used in constructing the centroid of pulses that trigger the high threshold. The charge amplitude measurement is provided by the duration of low-threshold comparator's time-over-threshold, which, in a full implementation of the ASIC, would be stored digitally in an on-board FIFO and read out asynchronously. The chip includes a power-cycling feature that is designed to allow the chip to be powered on in 1 msec, allowing the chip to reduce its power consumption by 99% by exploiting the 5 Hz duty cycle of the Linear Collider. The time-over-threshold digitization of the charge amplitude allows for real-time processing of minimum-ionizing signals, with no dead time other than that associated with the return-to-baseline of the amplified pulse. Due to its real-time processing of pulse-height information, which limits occupancy-related deadtime, the LSTFE time-over-threshold strategy is a particularly promising approach for the use of microstrips for forward tracking.

1.1.6 Simulation Infrastructure

The vertex detector and tracker designs have been incorporated in the compact *xml* detector description that drives our simulation studies. This detector description serves as an input both to *slic.org*, the GEANT4-based detector simulation used by SiD, as well as the event reconstruction software.

The current detector description includes both the active sensing elements, as well as our estimates of the dead material required to provide mechanical support, beam tube, readout electronics, and required services (including power and cooling). For the tracking

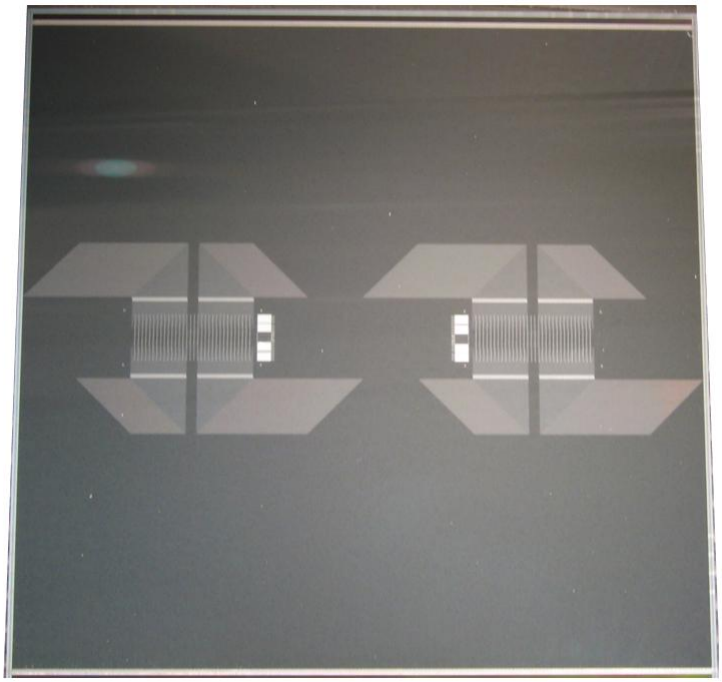

Figure 1.10: Photograph of a prototype SiD tracker sensor.

studies reported here, the barrel sensors have been approximated by thin cylinders, while the disk sensors have been approximated by planar disks perpendicular to the beamline. The dead material is modeled as a cylinder, planar disk, or cone as appropriate. Fig. 1.15 shows an x-y quarter view of the tracking system as implemented in this simplified geometry. This model has also been used to simulate the detector response for the large number of events generated for the physics benchmarking. Further details of the detector model are, therefore, presented in that section.

We have also developed a fully detailed tracker description that closely matches the engineering designs. It incorporates each individual sensor as a planar device with its mounting hardware. The fully segmented tracker description provides a highly realistic model of the tracker geometry, allowing us to study the effects of sensor overlaps and gaps, sensor mis-alignment, support material and more generally improve the precision of our detector modeling. Having the complete geometry fully defined and configurable at runtime (using a plain-text file), and immediately available to the reconstruction software, provides enormous flexibility to the design and optimization process.

Figs. 1.16 and 1.17 show the sensor layout for the fully segmented vertex detector and the sensor layout and support barrels for the central region of the fully segmented tracker description, respectively, as extracted from the GEANT4 description.

We do not include the individual pixels and strips in the GEANT4 simulation, preferring to defer this to the reconstruction stage. Instead, we store the full Monte Carlo information about the particle's interaction with the sensitive sensor material (e.g. track ID, deposited

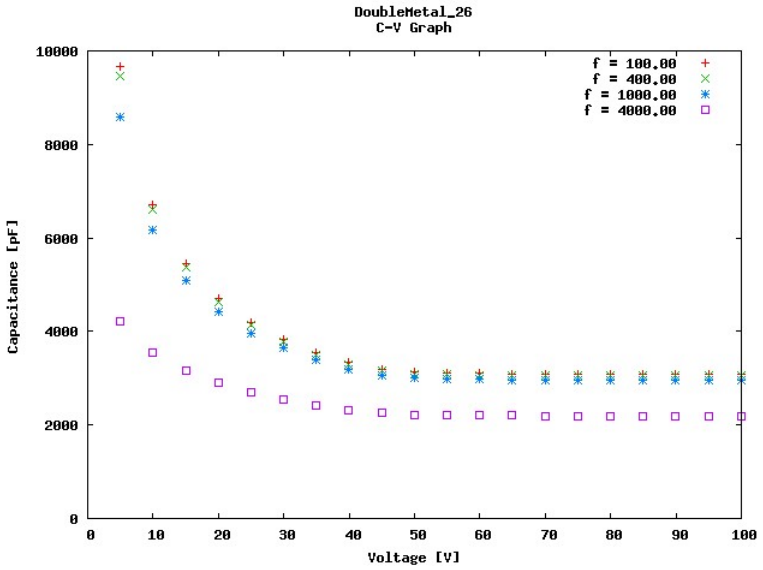

Figure 1.11: Capacitanc in pF versus bias voltage in Volt of a typical SiD double-metal prototype sensor.

energy, time, position). Hit digitization is the process of transforming these GEANT4 energy deposits into strip and pixel charge depositions, and then clustering these charge depositions to form tracker hits. This allows us to study different readout configurations without the overhead of having to rerun the full simulation.

1.1.7 Vertex Detector Hit Digitization

Although no baseline sensor technology has been established for the vertex detector, two vertex detector sensor simulation algorithms are currently implemented. The first one is based on a CCD simulation from SLD and is used in the simulation studies described here, which employs a cylindrical geometry. The second simulation package is more detailed and was developed for a more realistic planar geometry.

The main process to be simulated in a CCD is the diffusion of the charge from a charged particle track. In a CCD the larger part of the active layer is not depleted. That is, there is no electrical field in that part of the sensor and the charge collection occurs because of a slow diffusion of the charge into the CCD channel. In this case transverse diffusion has the same scale as the un-depleted layer thickness. To simulate the diffusion, a Gaussian distribution of the probability of an electron, generated at some point deep in the active layer, to reach the collection point a certain distance away from the projection of the generation point was assumed. The width of this distribution is proportional to the depth of the generation point. To be more precise, the model assumes two Gaussian distributions. The first one is for electrons that diffuse directly towards the CCD channel. The second distribution is for electrons reflected at the epitaxial layer, the substrate boundary, where there is a potential barrier. An important role in the performance of a tracking detector is played by the generation of the δ-electrons, that is, large energy transfer by the ionizing

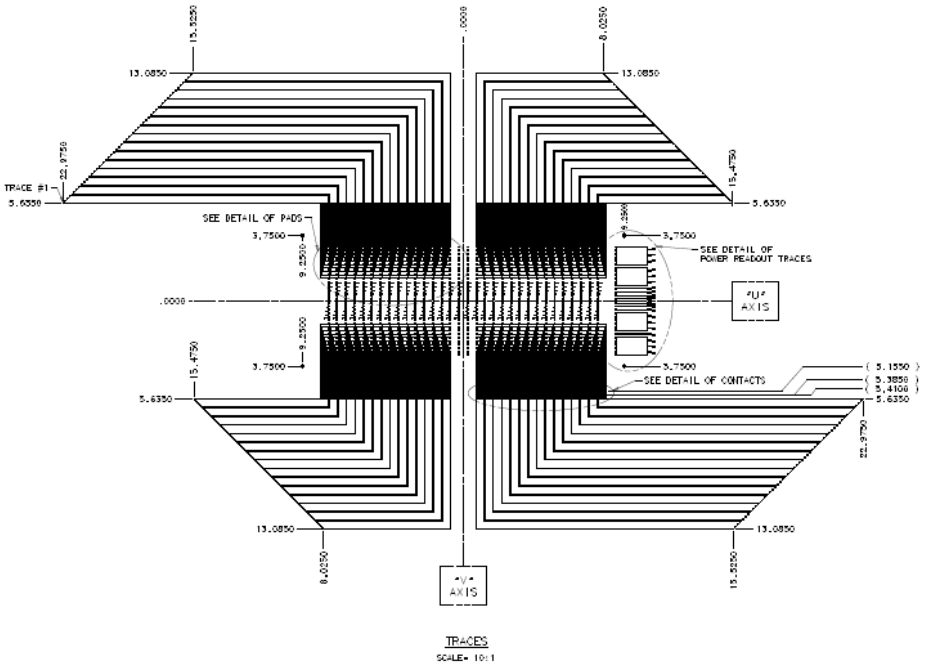

Figure 1.12: Detail of the double-metal routing of the traces to the readout chip and the connections to the readout cable, visible to the right of the bump-bond array.

particle to a single electron. This effect has been simulated by assuming that the energy loss in the tail of the Landau distribution is due to such δ-electrons. The width of the Landau distribution is simulated according to an empirical formula, which is in good agreement with experiment to thicknesses as small as about 10μm of silicon. The simulation package also includes special functions for simulating low-energy electrons, such as Compton electrons generated by photons.

Apart from the physics effects in the silicon detector, its performance is affected by the noise level of the readout electronics and the parameters of the signal digitization. All these effects have been simulated. This package does have its limitations, however, and was not designed for detailed studies of sensor effects. For example, it does not take into account specific effects in the energy loss in very thin layers ($\approx 1\mu$m). This effect as well as full simulation of diffusion and drift of charge carriers in any configuration of electric and magnetic fields inside the sensors are taken into account in second simulation package, which is described below.

The CCD simulation package starts with an initialization procedure that defines the CCD simulation parameters and geometry. At that time lookup tables are generated for the simulation of electron diffusion. The actual movement of each electron is not simulated in this package. Rather precalculated density functions for the distribution of electrons generated at a given depth inside the active layer are used. The next step in the simulation includes processing of every hit in the CCD detector. For every such hit, first the CCD and the pixel in the CCD is found where the hit is located. The CCD active layer is then divided into thin sublayers and the energy deposition in every sublayer is simulated. If the energy deposition

Parameter	**Value**
Overall Dimensions	93.531×93.531 mm^2
Active Area	92.031×92.031 mm^2
Strip pitch	25 μm
Readout pitch	50 μm
Number of strips	3679
Number of readout strips	1840
Depletion voltage	<100V
Biasing scheme	R_{poly}
Poly resistor value	20-40MΩ
Implant strip width	8 to 9 μm
Width of Al sense strips	8 to 9 μm
Width of double-metal readout traces	3 to 4 μm
Resistivity of Al sense strips	$< 25\Omega$/cm
Resistivity of double-metal readout traces	$< 60\Omega$/cm
Insulation thickness between metal layers	0.9 μm
Coupling capacitor value	> 10 pf/cm
Passivation (except bonding areas)	SiO_2, 0.5-1.0μm thick
Width of unpassivated regions on bias ring	$\geq 200\mu$m
Junction breakdown	> 200 V
Micro-discharge breakdown	> 150 V
Coupling capacitor breakdown	> 100 V
Total detector current at 150V	$< 4\mu$A
Interstrip capacitance	< 1.2 pf/cm

Table 1.4: Specifications for some of the SiD sensor parameters.

in any sublayer is in the tail of the Landau distribution, the generation of a δ-electron is assumed. The charge is propagated to the CCD surface according to the diffusion density functions, and charge signals in the central pixel, as well as in neighboring ones are found. The electronics noise is then added, and the ADC digitization algorithm is applied. The resulting ADC outputs for all pixels in the CCD are fed to the cluster finding routine, which finds clusters of pixels and the coordinates of their centers. Different algorithms may be used for coordinate finding. For the current studies a charge weighted average clustering algorithm is used. It should be noted that, although the name of the package implies simulation of CCDs, the package is rather versatile. By changing the parameters of the simulated sensor and by setting appropriate depletion depth and bias voltage, other types of silicon sensors can be simulated.

In a second, more detailed simulation package, the parameterization of the diffusion and

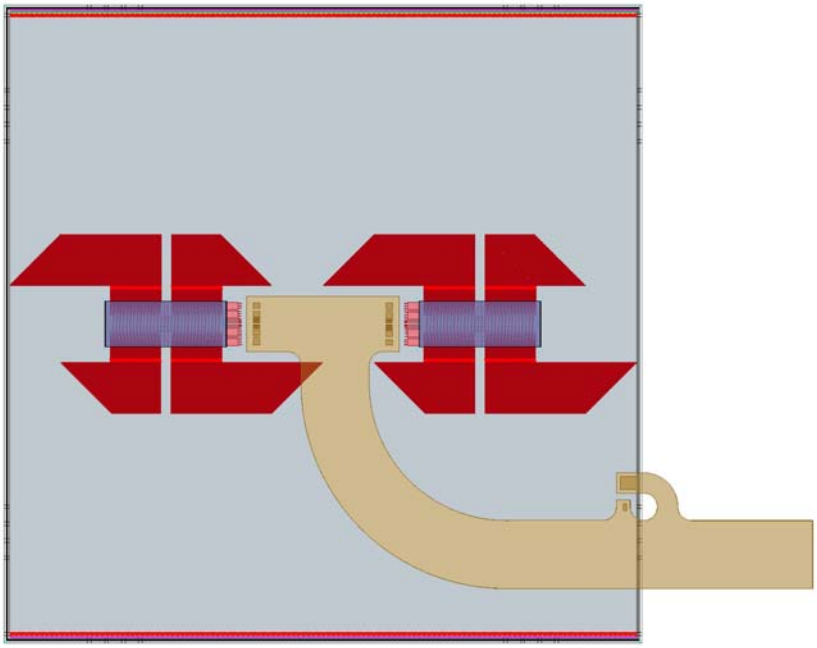

Figure 1.13: An x-ray view showing the details of the sensor readout chain for tracker modules.

the approximation of the Landau distribution has been eliminated. This package simulates every ionizing collision of a relativistic charged particle travelling through the sensitive layer of silicon. Algorithms and functions, developed by Hans Bichsel, were used to simulate interaction points and the energy losses of such collisions. If the energy loss exceeds a few keV, the generation of a δ-electron is assumed. If it is not a δ-electron, all electron-hole pairs generated in this collision are assumed to originate at the collision point. If it is a δ-electron, a random vector is generated for its direction and the path length of its trace is taken from a range table for low energy electrons in silicon. For each electron or hole, depending of the type of signal generating carriers in the given sensor, the drift and diffusion in the sensor volume is simulated. Electric and magnetic maps are used to simulate the path of each single carrier. The sensor geometry description defines the regions where carriers are collected. These simulation studies not only provide the signal amplitude in each pixel, but also the signal shape and time of the charge collection.

Detailed simulation takes a lot of computing resources. To enable physics benchmark studies, lookup tables are used, which tabulate the probability for each pixel to collect charge as function of the impact point inside the pixel under consideration or in a neighboring pixels. When using lookup tables, the timing of the charge collection is also simulated, though it is less accurate than in the case of the detailed simulation of carriers propagation. In addition to the probabilities of the carriers generated at a given space point to be collected by given pixel, the average time of such collection is also tabulated. This information can then be used at a later stage to generate the distribution of arrival time for carriers from given point inside a pixel. The shape of the distribution may change, however, depending on the electric field map and a correction may need to be applied based on the detailed simulation.

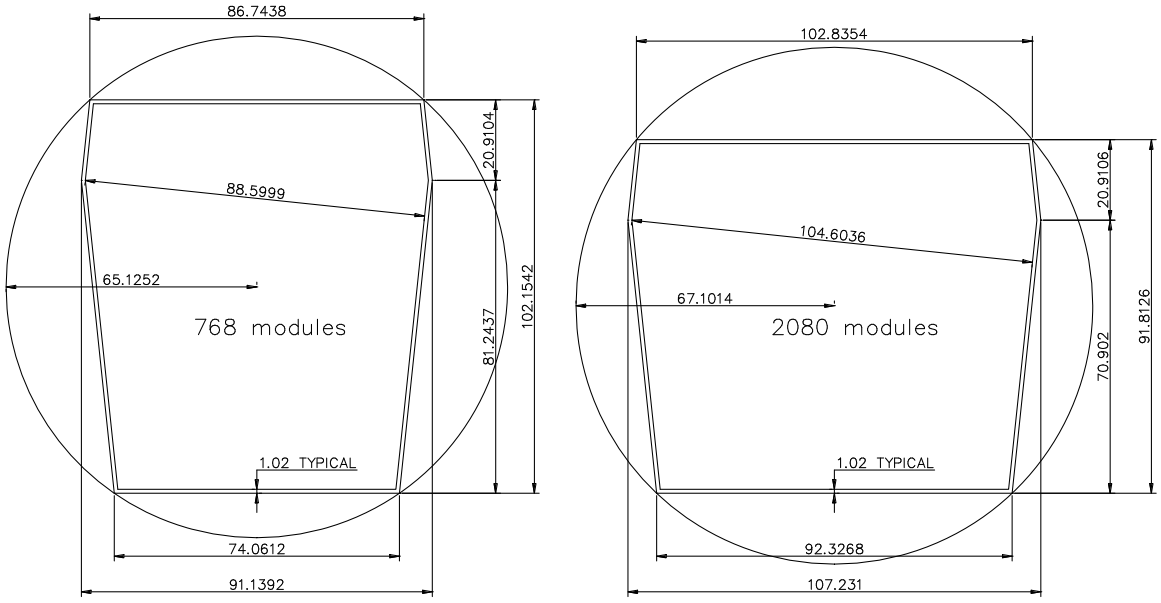

Figure 1.14: A proposed pair of sensor designs for the endcap modules of the SiD tracker. Strips are parallel to one of the long edges of each sensor. Placed back-to-back around a support frame, they create a stereo pair. The sensor and module design details are essentially identical to the barrel prototypes.

In addition to digitizing real particle hits, the simulation package also provides the possibility to generate fake hits from the electronics noise. Signal processing for different technologies may be different and the simulation can use amplitude and time information as appropriate.

1.1.8 Tracker Hit Digitization

The requirements for digitization of hits in the microstrip sensors of the tracker are somewhat different than for the thin pixel sensors of the vertex detector. Above about 100 μm in thickness, there is no need to simulate straggling effects or drift each charge carrier generated in the silicon individually. In addition, recent versions of Geant4 do an excellent job of simulating the charge deposition and generating δ-rays in these layers, simplifying the simulation of charge deposition at reconstruction time considerably.

Two different strategies are used for digitization of hits in the outer tracker depending upon the geometry being simulated. For the cylindrical geometries used in physics benchmarking a "virtual segmentation" is performed to divide the cylinder into individual tiles that are roughly the same size as single modules. In this case, the deposited charge is calculated directly from the energy deposition generated by Geant4 and the location of the charge deposition is smeared according to a Gaussian in the measured coordinate. The length of a hypothetical strip located at that coordinate is calculated in order to constrain tracks in the unmeasured coordinate.

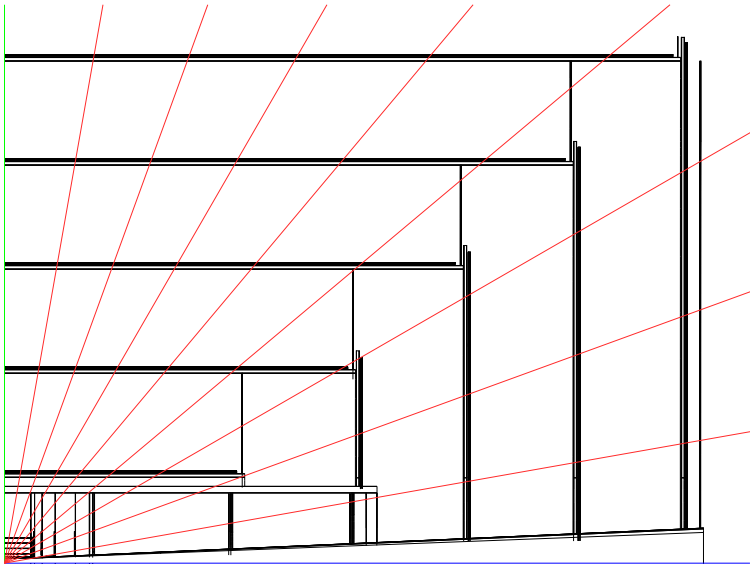

Figure 1.15: R-z view of the simplified tracking system as implemented in SiD02.

In the more realistic detector model with individual planar sensors, a more sophisticated charge deposition and digitization package is used to accurately simulate the hits that would be produced in the real detector. This model is used for more detailed tracking studies to optimize the design and validate the underlying tracking performance of the simplified digitization and detector geometry used for physics benchmarking. There are three components of this full digitization package for the outer tracker: charge generation and deposition, response of the readout system, and clustering of hits into measurements.

The charge is generated according to the energy deposition by Geant4 with small range cuts (a few μm) and step sizes (of order 50 μm) to produce an accurate description of the spatial distribution of the generated charge. The paths along which charge is generated are then subdivided into pieces no longer than a few microns, and the cloud of charge from each piece is drifted to the surface of the sensor according to the applied electric and magnetic fields including diffusion effects. At the surface of the sensor, the Gaussian-distributed cloud of charge is integrated onto the detailed pattern of electrodes from all of the hits in an event. The charge is then transferred from the sense strips to the AC-coupled readout strips according to the ratio of the coupling capacitance to the total capacitance of each sense node. This is important to accurately estimate the charge collection efficiency of the "intermediate strips" between each strip that is instrumented with a KPiX channel. A complete register-level model of the KPiX chip has been implemented to convert the charge on each readout strip to a digital signal: this is critical to understanding the impact of KPiX design decisions on the performance of the tracker, which sits at the small-signal extreme of the palette of KPiX applications. The simulation of KPiX includes full modeling of the noise of each readout node according to its capacitance, and Gaussian noise is added to all strips that will be detectable given the clustering algorithm being used. Clusters are seeded with channels above some threshold, typically four standard deviations of noise above the pedestal, and channels above

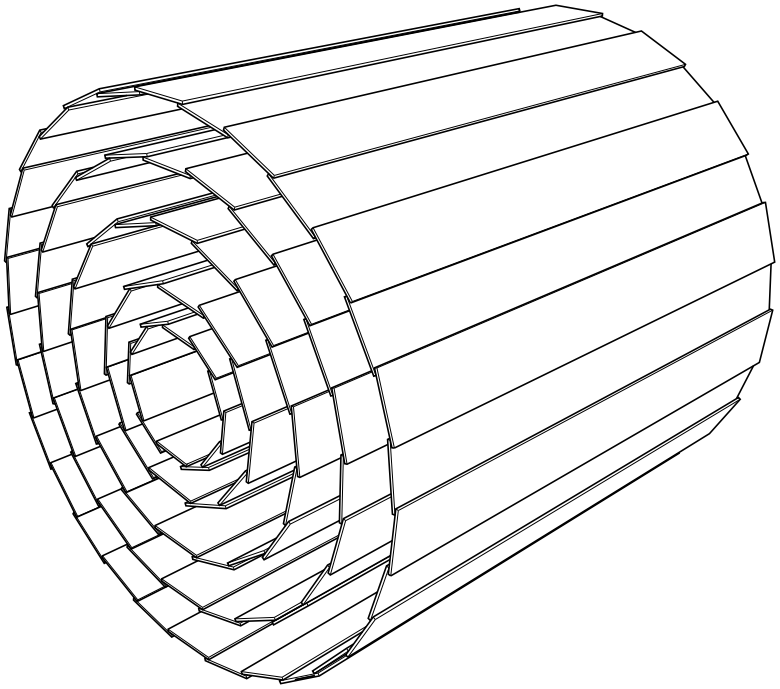

Figure 1.16: The central vertex detector showing the layout of the silicon pixel sensor modules.

some lower threshold, typically two standard deviations of noise above pedestal, are added to complete the clustering of each hit. The measured coordinate of clusters with three or fewer strips is taken as the charge-weighted centroid of those strips, while the charge on interior strips of longer clusters is first averaged over all of the interior strips to minimize the degradation of cluster position due to fluctuations in energy deposition and noise for tracks that cross the silicon at shallow incidence angles. The length of a hypothetical strip at the charge-weighted centroid is used to constrain the non-measured coordinate. Fig. 1.18 shows the hits resulting from this simulation in the double-sided endcap modules of the SiD tracker. Hits in green trace their parentage to generated Monte Carlo particles while those in purple result from readout noise.

1.1.9 Track Reconstruction

The standard pattern recognition algorithm developed by SiD is designed to efficiently find tracks using pixel and strip hits in the tracker. The pattern recognition algorithm treats the tracker as a single integrated device that is "agnostic" as to the origin of the hits (pixel or strip, barrel or endcap). This approach provides uniform pattern recognition throughout the tracking volume, effortlessly handling transitions between the different parts of the detector. Typically, 6-7 hits are sufficient for finding a track, which allows the standard pattern recognition algorithm to efficiently track particles originating near the interaction point with $p_T > 200$ MeV.

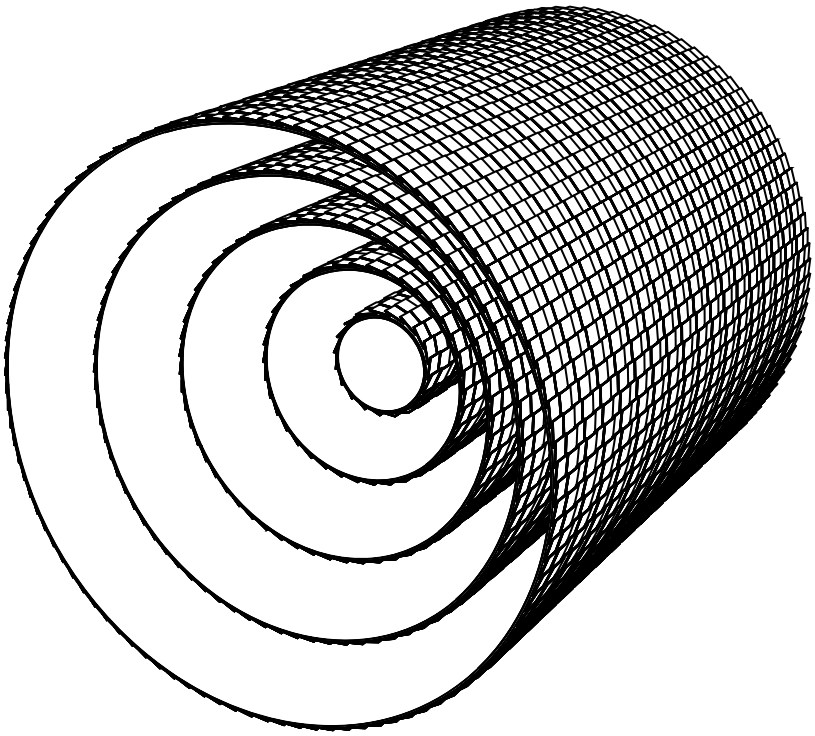

Figure 1.17: The central tracker showing support barrels tiled with overlapping readout modules.

Since pattern recognition is of utmost importance in a sparse hit environment, additional track finding algorithms are explored. Of particular note is the calorimeter assisted track finder, which uses the tracking capability of the electromagnetic calorimeter to associate hits in the outer tracker with calorimeter "track stubs". Calorimeter assisted tracking is particularly well suited to reconstructing tracks that originate outside the vertex detector, as often occurs in K_s and Λ decays. Both the standard pattern recognition and calorimeter assisted tracking algorithm are described below.

1.1.9.1 Standard Pattern Recognition Algorithm

The standard pattern recognition algorithm is explicitly designed for the task of optimizing the design of an all-silicon tracker. Variations in tracker geometry and layout can be easily studied with no change to the software. The algorithm bases all its decisions on a global χ^2. A high level of user control over the tracking "strategies" is available if desired, but more typically a "strategy builder" tool is used to automate the process of developing an optimized set of strategies for a given detector configuration.

The first step in track finding is to convert the digitized hits into a common hit format. This format encapsulates all the information needed by the standard pattern recognition algorithm, while insulating the track finding from differences and changes in the digitization

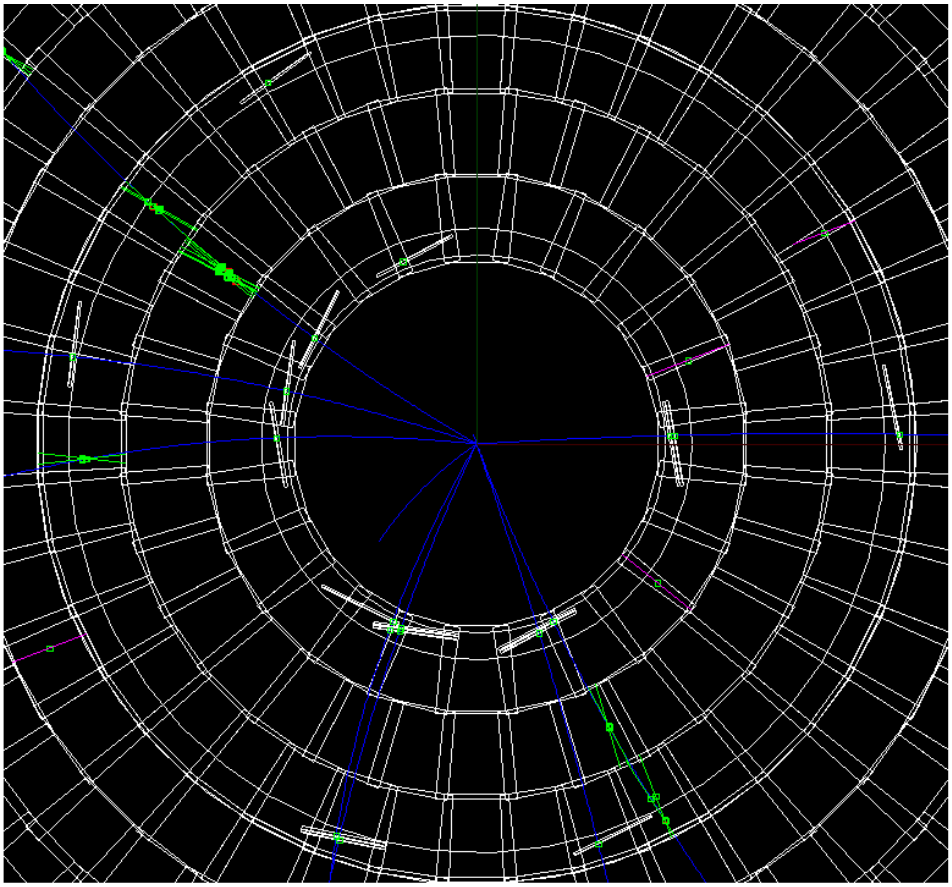

Figure 1.18: Hit pattern in the tracker disks.

algorithms.

Three types of hits are supported: pixel hits that have two measured coordinates, axial strip hits that have one measured coordinate and one bounded coordinate, and stereo hits formed from a pair of strip hits. The pixel and stereo hits may be associated with either barrel or disk geometries, while the axial strip hits have the bounded coordinate parallel to the beam axis and are intrinsically associated with barrel geometries. One further limitation is placed on stereo hits: the planes of the two strip sensors must be parallel to each other.

Track finding is controlled by a set of strategies. A strategy consists of the list of detector layers to be used, the role of each layer (seed, confirm, or extend), kinematic constraints (p_T, impact parameters), requirements on the number of hits, and the χ^2 cut. Multiple strategies can be processed by the track finding algorithm, and the resulting tracks are the collection of all distinct tracks found. The set of strategies is contained in an *xml* file that is easily understood and can be viewed/edited with a text editor.

The track finding algorithm is exhaustive in the sense that all combinations of hits that could potentially lead to a successful track fit are considered. The algorithm proceeds in four steps:

1. The first step is to form a 3-hit track seed candidate by taking all 3-hit combinations possible among the 3 seed layers. A helix fit is performed on the seed candidate, and those seeds that fail the χ^2 cut are eliminated.

2. The second step tries to "confirm" the seed by adding additional hit(s) from the confirm layer(s). A helix fit is performed on the new seeds and those that fail the χ^2 cut are eliminated. Typically, it is found that good performance is achieved with one confirmation layer.

3. The third step seeks to "extend" a confirmed seed by trying to add additional hits from the extend layers. Each time a new hit is considered, a helix fit is performed and the hit is discarded if it fails the χ^2 cut. If no hits in a given extend layer give a satisfactory helix fit, then the original track seed is kept and the next extend layer is tried.

4. Track seeds that meet the strategy's requirement on the minimum number of hits are merged to form a list of distinct tracks. Two track candidates are allowed to share a single hit, but if a track candidate shares more than one hit with another candidate, an arbitration scheme is used to select the better candidate. Precedence is given to the candidate with the greatest number of hits, while the candidate with smaller χ^2 is selected when the number of hits is equal.

Consistency checks and hit sorting algorithms are used to minimize the number of helix fits performed, substantially improving the performance of the algorithm. Furthermore, a "bad hit χ^2" cut is used to identify track candidates with an outlier hit and allows preference to be given to track candidates without an outlier hit.

A key component of the pattern recognition algorithm is a fast helix fitter. The helix fitter takes as input 3 or more tracker hits. The hits can be any combination of pixel, axial strip, or stereo hits in the barrel and/or endcap detectors. The fitter is the one place in the tracking code that distinguishes between the various types of hits. The fast fitter is used to estimate the helix parameters and helix fit χ^2. First, a circle fit to the x,y coordinates of all hits is performed using the Karimäki algorithm to determine the helix parameters ω, ϕ_0, and d_0. If there are two or more pixel/stereo hits, then a line fit in the $s-z$ plane is used to determine the z_0 and $\tan\lambda$ helix parameters. In order to provide full helix fits for the case where there are fewer than two pixel/stereo hits, a new fitting algorithm was developed.

While an axial strip does not measure the z coordinate, it has well defined bounds that impose the constraint $z_{min} < z < z_{max}$. These bounds lead to each axial strip having an allowed band in the z_0-$\tan\lambda$ plane. For two or more axial strips, the intersection of these bands will produce a polygonal allowed region, the centroid of which is taken to be the measured values for z_0 and $\tan\lambda$. If there is no region of intersection, the hits are inconsistent with being from a helix and the fit fails. For the case of a single pixel/stereo hit, the pixel/stereo hit is treated like a very short strip and the above algorithm is used.

For all but the highest momentum particles, the multiple scattering errors will exceed the intrinsic hit resolution. Multiple scattering errors for both the active and dead materials are estimated and included in the helix fit. Correlations in the multiple scattering errors are ignored, leading to an under-estimate of the helix parameter errors by a factor of ≈ 1.5.

For stereo hits, full account is taken for the separation between the two stereo layers in the calculation of both the hit position and hit covariance matrix.

The performance of the standard pattern recognition algorithm is shown in the section on tracker performance and is also reflected in the benchmarking studies. Unless otherwise noted, the tracking strategies require 1 confirmation hit, a total of at least 7 hits (6 hits for barrel-only tracks), $p_T > 0.2$ GeV, xy distance of closest approach $d_0 < 10$ mm, and distance of closest approach along the beam direction $z_0 < 10$ mm.

1.1.9.2 Calorimeter-Assisted Tracking

The development of the calorimeter assisted track finding algorithm was primarily motivated by the need to reconstruct non-prompt tracks and long-lived particles in the SiD detector. As will be shown later, the standard track finding algorithm achieves excellent efficiency in reconstructing prompt tracks that originate close to the interaction point. However, using the same algorithm for finding non-prompt tracks is difficult because those tracks often do not produce enough hits in the vertex detector to seed the track finder, and creating seeds from 3-hit combinations in outer layers without limiting combinatorics by constraining the track origin to the interaction region can be problematic.

The calorimeter assisted tracking solves the problem by seeding the track finder from traces left by charged particles in the electromagnetic calorimeter - so called MIP stubs. The standard SiD track finder is run first, and the found tracks are then propagated through the calorimeter. Clusters are created and attached to the tracks. After that, topological clustering is applied to the remaining calorimeter hits. Those of the created clusters that include hits in inner electromagnetic calorimeter layers are analyzed for consistency with being produced by minimum ionizing particles. Clusters that pass the test are converted into track seeds that contain information about the track position and direction at the calorimeter entry point. Depending on the MIP stub quality, the seed can also contain a track curvature estimate. The seeds are propagated back into the tracker, picking up hits that are not attached to any existing tracks. The search window in each tracker layer is calculated based on the trajectory parameters uncertainties, and the track parameters are re-evaluated after attaching every new hit. If more than one hit can be attached to the track in a certain layer, multiple track candidates are created. Once all seeds have been processed, the newly created tracks are rated based on quality, and duplicates are removed. This algorithm is essential for reconstructing all kinds of non-prompt tracks - K_s^0 and Λ decay products, new physics signatures that might include long-lived particles, kinked tracks, and calorimeter backscatters. It also performs high purity, topologically linked initial clustering in the calorimeter, and associates clusters with tracks.

1.1.9.3 Track Fitting

The track fitting results presented here use the fast helix finder described before. Two more precise approaches to track fitting have been developed by SiD. The first of these is based on a track fitting algorithm originally used by SLD and used in previous studies of the

performance of the SiD tracking system. It solves minimization equations for χ^2, calculated from the matrix of residual weights. This weight matrix takes into account multiple scattering derived from the amount of material passed by a track, correlations between track deviations in the subsequent detector layers and independent measurement errors due to the sensors spatial resolution. Solving the matrix equation for 5 track parameters gives the parameter values corresponding to the best fit; the inverse of the weight matrix of the parameters gives the covariance matrix of parameter errors. Comparison of the expected parameter errors derived from the covariance matrix with real track parameter residual distributions shows agreement to within a few percent. This fitter may be slow for a large number of layers, as it requires a matrix inversion with a matrix dimension equal to the number of layers. For the SiD concept, however, it works fine as total number of layers crossed by a track rarely exceeds 10. A Kalman filter, which treats multiple scattering close to optimally, is under development and updated results using that Kalman filter will be presented at a later time. The Kalman filter will be used as a final fitter to refit tracks that are currently fitted by the simple fitter.

1.1.10 Tracking Performance

In this section the performance of the vertex and tracking detector will be described, along with its associated track-parameter fitter. The goal of these studies is to evaluate the overall performance of the SiD tracking system with the most realistic simulation available. The standard tracking algorithm was tuned for the benchmark processing to find tracks having $p_T > 0.2$ GeV that originate from near the interaction region. The strategies used generally required at least 7 hits to be associated with a track. An additional strategy that required 6 barrel hits in the vertex detector and first layer of the outer tracker was put in place to provide low-p_T coverage for central tracks that may not pass through 7 different layers before curling back around. Additionally, for the benchmark processing the strategies placed a 1 cm constraint on the x-y and z distances of closest approach.

We can break down tracking efficiency into two parts: (1) the fraction of Monte Carlo charged particles that are in principle "findable" given the set of strategies used, and (2) the track reconstruction efficiency for the findable tracks. The starting point for the tracking efficiency measurement is the set of long-lived charged particles identified as being "final state particles" by the event generator. Final state particles include short-lived particle decay products (e.g. $\pi^{\pm}$ from $K_S \to \pi^+\pi^-$), but does not include long-lived particle decay products (e.g. $\pi^{\pm}$ decay products) or secondaries produced by GEANT as the result of interactions in the detector.

Among the final state particles in $e^+e^- \to t\bar{t}$ collisions at $\sqrt{s} = 500$ GeV, 6.5% of the tracks are below the 0.2 GeV p_T cutoff in the standard tracking algorithm. Of the tracks satisfying the p_T constraint, 9.1% of the tracks have fewer than 6 hits, which is the minimum number of hits for the standard tracking algorithm. Some of these tracks are from sources, such as K_s decay, that are potentially recoverable by the calorimeter assisted tracking algorithm. Findable tracks must also satisfy the requirements for having seed and confirmation hits and satisfy the 1 cm constraint on the x-y (d_0) and z (z_0) distances of closest approach. Taken together, 84.4% of the final state particles are findable by the standard

Selection	Selection Efficiency	Cumulative Efficiency
All Tracks	-	100%
$p_T \geq 0.2$ GeV	$(93.54 \pm 0.11)\%$	$(93.54 \pm 0.11)\%$
$N_{hit} \geq 6$	$(90.91 \pm 0.13)\%$	$(85.04 \pm 0.16)\%$
Seed Hits Present	$(99.78 \pm 0.02)\%$	$(84.85 \pm 0.17)\%$
Confirm Hit Present	$(99.95 \pm 0.01)\%$	$(84.84 \pm 0.17)\%$
$\lvert d_0 \rvert \leq 1$ cm	$(99.80 \pm 0.02)\%$	$(84.65 \pm 0.17)\%$
$\lvert z_0 \rvert \leq 1$ cm	$(99.69 \pm 0.03)\%$	$(84.39 \pm 0.17)\%$
Track Reconstruction	$(99.32 \pm 0.04)\%$	$(83.81 \pm 0.17)\%$

Table 1.5: Fraction of findable tracks

tracking algorithm. The breakdown of these contributions to the findable track efficiency can be found in Table 1.5.

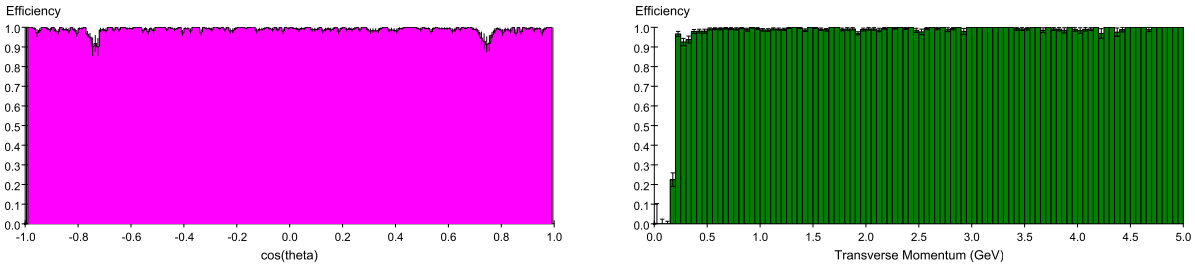

Figure 1.19: Track finding efficiency as a function of track $\cos\vartheta$ (left) and p_T (right).

The track reconstruction efficiency measures the fraction of findable tracks that are found by the standard tracking algorithm. Using the sample described above, the track reconstruction efficiency is found to be 99.3%. Fig. 1.19 shows the efficiency as a function of $\cos\vartheta$ and p_T. The track finding efficiency drops in the transition region between barrels and disks. Fig. 1.20 shows the efficiency as function of $\cos\vartheta$ for two p_T bins. The left plot is for tracks with $p_T < 500$ MeV and the right plot is for tracks with $p_T > 500$ MeV. All the inefficiency is due to low momentum tracks in this transition region. It is thought that the inefficiency is due to tracks just beyond the pixel barrel acceptance that curl by more than 180 degrees before they get to the seed layers that cover this acceptance region. As such, this may be an artifact of the current tracking algorithm and could be improved upon.

Tracking algorithms must balance track finding efficiency against the probability of finding "fake tracks" that are not associated with a Monte Carlo particle. A key indicator for the number of fake tracks is the number of mis-assigned hits on a track. These hits are generated by a different Monte Carlo particle than the one with the preponderance of hits on the track. More than 99% of tracks have at most one wrong hit on the track, as seen from Fig. 1.21. Fake tracks, where no single Monte Carlo particle is responsible for the majority of hits, make up only 0.07% of the tracks found.

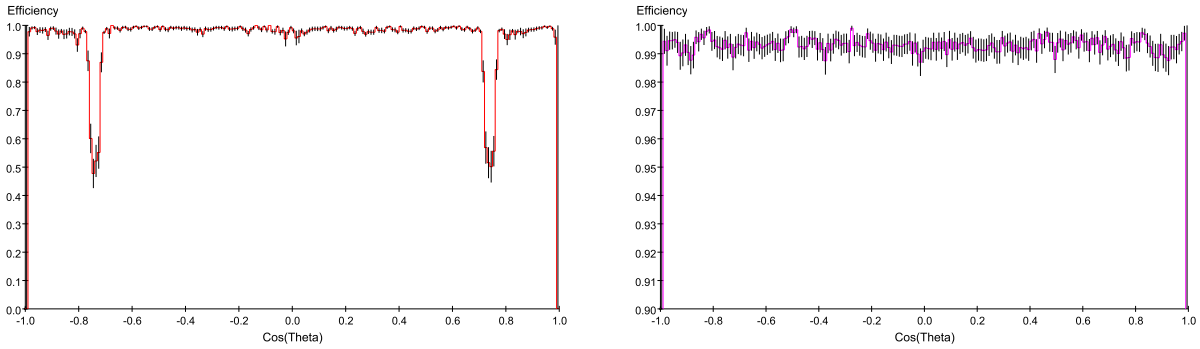

Figure 1.20: Track finding efficiency as a function of track $\cos\vartheta$ for tracks with $p_T < 500$ MeV (left) and $p_T > 500$ MeV (right). Please note the different vertical scales in the two figures.

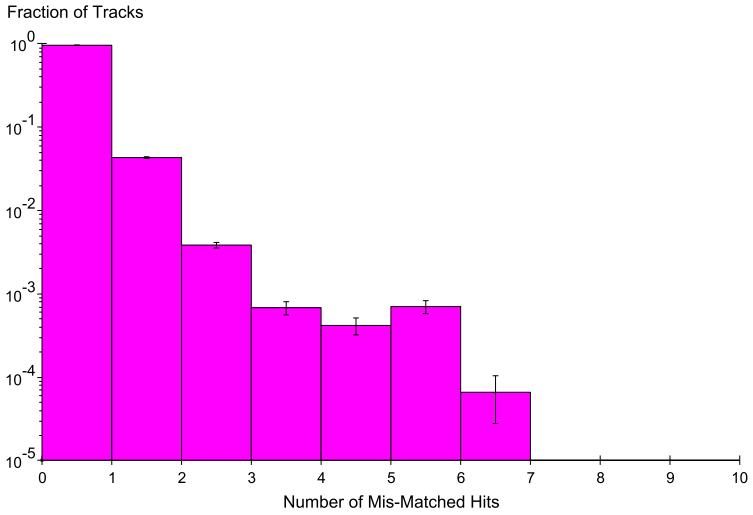

Figure 1.21: Fraction of tracks versus the number of mis-assigned hits.

The momentum resolution of the tracker is shown in the top plot in Fig. 1.22 as a function of momentum for various track angles. The bottom figure shows the impact parameter resolution for various track angles. An impact parameter resolution of 4 μm is obtained in the high momentum limit.

How the tracking performs in higher occupancy environments is summarized in Fig. 1.23. Two studies have been carried out. First, the performance of the track finder has been studied in the environment of dense jets. The plot in the upper left corner in Fig. 1.23 shows the track finding efficiency as function of the angle between the track and the jet thrust axis for $e^+e^- \to q\overline{q}$ events at $\sqrt{s} = 1$ TeV. The efficiency holds up rather well, dropping by about 1% for tracks within 2mrad of the jet core. The distribution in α, the angle of charged particles with respect to the jet thrust axis, is shown in the upper right corner in Fig. 1.23. The bottom figure shows the track finding efficiency as a function of track p_T for $e^+e^- \to b\overline{b}$ events at $\sqrt{s} = 500$ GeV with the backgrounds from 10 bunch crossings overlaid. In this

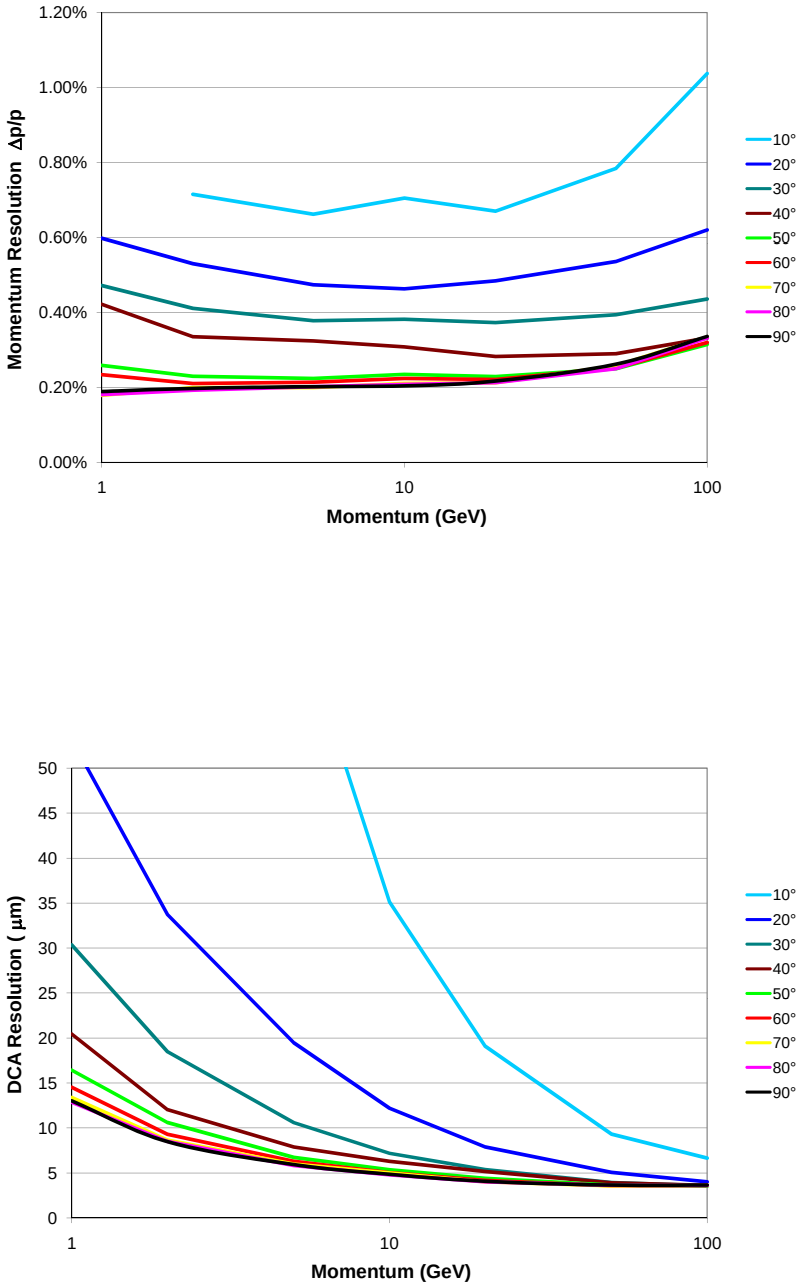

Figure 1.22: Resolution in momentum (top) and $r - \varphi$ distance of closest approach, DCA (bottom), as function of track momentum at various angles.

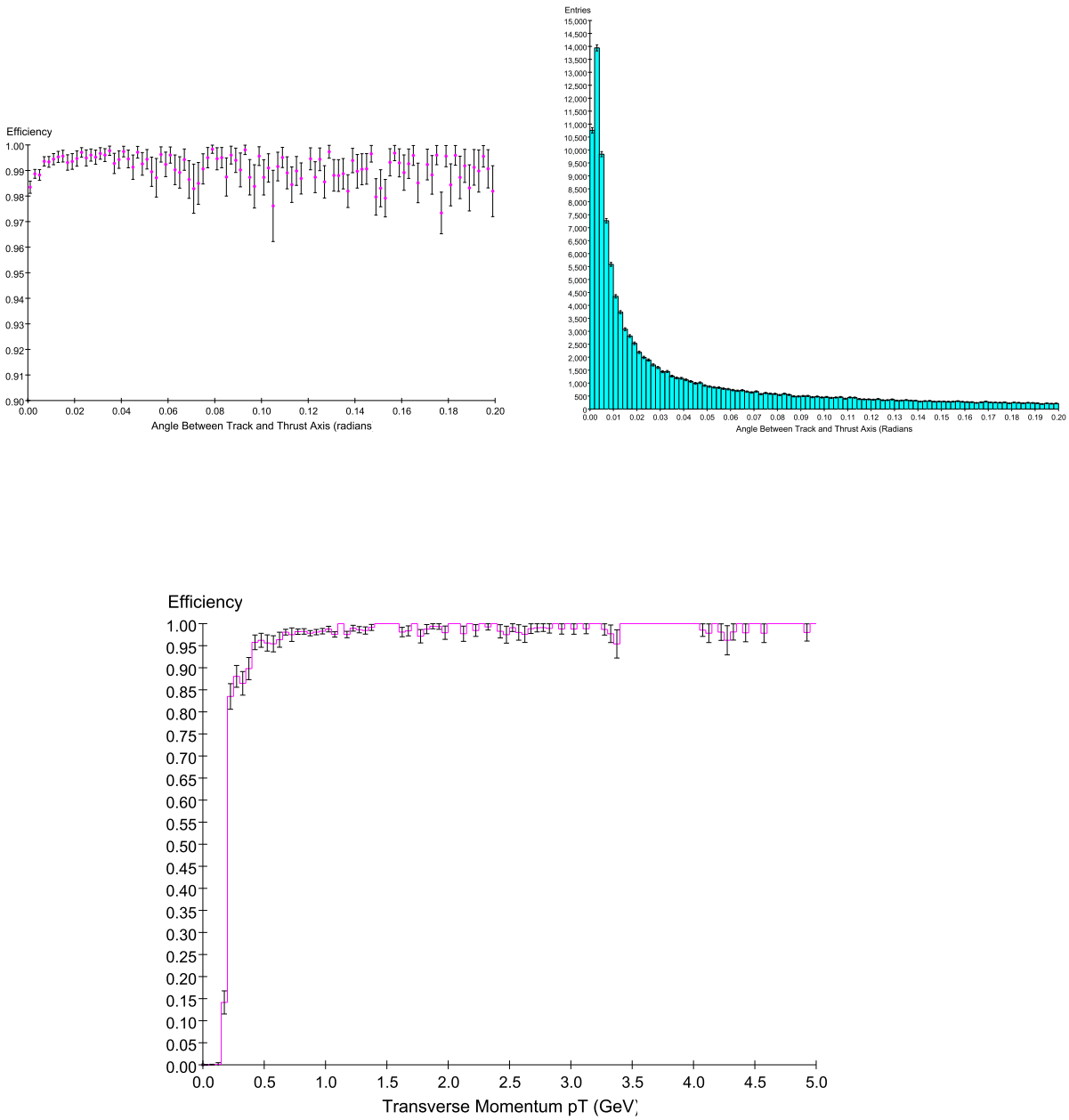

Figure 1.23: Tracking efficiency as function of α (upper left) and distribution in α (upper right) for $e^+e^- \to q\overline{q}$ events at $\sqrt{s} = 1$ TeV. The bottom figure shows the tracking efficiency for $e^+e^- \to b\overline{b}$ events at $\sqrt{s} = 500$ GeV with the background from 10 bunch crossings overlaid.

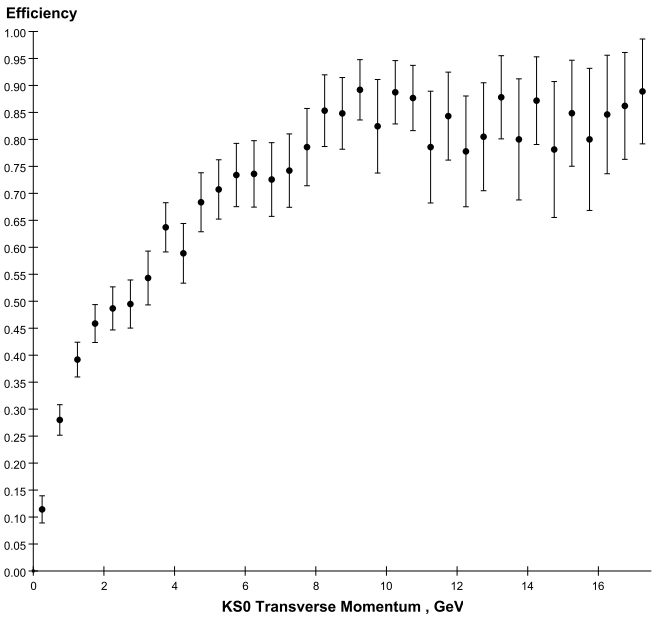

Figure 1.24: K_s^0 finding efficiency as function of its transverse momentum.

study the effect of accumulating beam backgrounds over 10 crossings has been mimicked by adding these hits to all pixel devices in the detector. Hits in the silicon strip tracker were added only for a single bunch crossing, in-time of course with the physics event. There is a small loss in efficiency at low p_T, as anticipated. Also the fake track rate is higher, about 0.6%. Most of the fake tracks seem to be due to combinatorics.

An often-voiced concern of a tracker with relatively few measurements on a charged particle trajectory is the efficiency for the reconstruction of long-lived particles. The SiD detector should be viewed as an integrated detector where the overall performance derives from a combination of all the subdetectors. As described in section 1.1.9.2 a calorimeter assisted track finding algorithm was developed to reconstruct non-prompt tracks and long-lived particles. Fig. 1.24 shows the K_s^0 reconstruction efficiency for $t\bar{t}$-events, obtained by running the standard tracking algorithm followed by the calorimeter assisted tracking algorithm. The efficiency is defined as the ratio of the number of successfully reconstructed K_s^0's to the total number of K_s^0's that decayed into a charged pion pair inside the third layer of the outer tracker. The efficiency reaches 85% for K_s^0's with transverse momenta above 8 GeV. The result represents the current status of the software and significant improvements, particularly for low momentum K_s^0, are anticipated.

All the simulations are performed using a uniform 5 Tesla magnetic field with no radial component. ANSYS simulations of the solenoid and the return flux show that the field is not uniform. Fig. 1.25 shows the distribution inside the tracking volume of the longitudinal (left) and radial (right) component of the magnetic field. The SiD detector having a 5 T magnetic field is defined as the field at $(R, z) = (0, 0)$ being 5 T. In Fig. 1.25 B_z is given as fraction of the nominal 5 T field. In the center of the detector B_z increases slightly with increasing

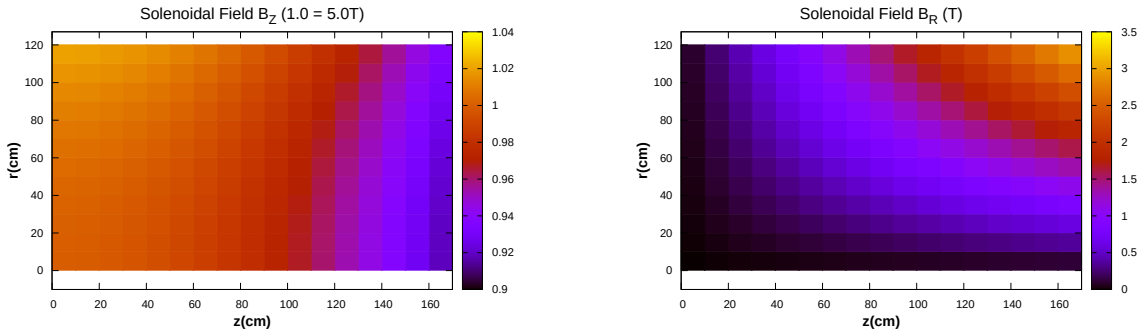

Figure 1.25: Map of the magnetic field components inside the tracking volume: B_z in fractional deviation from the nominal magnetic field (left) and B_R in absolute values (right)

radius. There is a drop of about 6% when reaching the end of the tracker volume. The field component B_R, given in absolute values in Fig. 1.25, is not negligible. The effect of a non-uniform magnetic field was studied by simulating particle trajectories with the field map as shown in Fig. 1.25 and reconstructing the trajectories assuming a perfect uniform field configuration. Preliminary studies indicate the effect on the pattern recognition to be minor. Studies are ongoing to investigate how it affects the fitted track parameters and whether the field uniformity must be improved.

1.1.11 Tracker Alignment

The unprecedented track momentum resolution contemplated for linear collider detectors demands minimizing systematic uncertainties in sub-detector relative alignments. At the same time, there is a strong impetus to minimize the amount of material in the tracking system, which might compromise its stability. These two requirements put a premium on accurate alignment of the various elements of the tracker. The short time scales on which alignment could change (e.g., from beam-driven temperature fluctuations) may preclude reliance on traditional alignment schemes based on detected tracks, where it is assumed the alignment drifts slowly, if at all, during the time required to accumulate sufficient statistics.

The prospect of two ILC detectors swapping places in the beamline only increases the importance of *in situ* alignment monitoring that does not depend on tracks. It will be important to monitor tracker distortions during the push-pull operations, not only for later track reconstruction, but also to ensure that no damage-inducing stresses are inadvertently applied to the tracker components. Alignment systems that can also be used during tracker assembly to monitor strains would also be useful.

A system that can monitor alignment drifts in real time would be highly desirable in any precise tracker and probably essential to an aggressive, low-material silicon tracker. The tradeoff one would make in the future between low material budget and rigidity will depend critically upon what a feasible alignment system permits. The SiD tracker is considering two

alignment methods, one based on Frequency Scanned Interferometry (FSI), and one based on Infrared Transparent Silicon Sensors (IRSS).

The FSI system incorporates multiple interferometers fed by optical fibers from the same laser sources, where the laser frequency is scanned and fringes counted, to obtain a set of absolute lengths. With a test apparatus the state of the art in precision DC distance measurements over distance scales of a meter under laboratory-controlled conditions has been reached and even extended. Precisions better than 100 nm have been attained using a single tunable laser when environmental conditions are carefully controlled. Precisions under uncontrolled conditions (e.g., air currents, temperature fluctuations) were, however, an order of magnitude worse with the single laser measurements.

Hence a dual-laser FSI system is foreseen for the tracker, that employs optical choppers to alternate the beams introduced to the interferometer by the optical fibers. By using lasers that scan over the same wavelength range but in opposite directions during the same short time interval, major systematic uncertainties can be eliminated. Bench tests have achieved a precision of 200 nm under highly unfavorable conditions using the dual-laser scanning technique. Fig. 1.26 shows an example of dual-laser fringes measured on a benchtop single-channel prototype system.

It should be noted that complementary analysis techniques of FSI data can be used either to minimize sensitivity to vibrations in order to determine accurate mean shape distortion or to maximize sensitivity to vibrations below the Nyquist frequency of data sampling. The latter algorithm could prove especially useful in commissioning in assessing vibration effects, such as might arise from pulse powering in a magnetic field.

The second method exploits the fact that silicon sensors have a weak absorption of infrared (IR) light. Consecutive layers of silicon sensors are traversed by IR laser beams which play the role of infinite momentum tracks (see Fig. 1.27). Then the same sophisticated alignment algorithms as employed for track alignment with real particles can be applied to achieve relative alignment between modules to better than a few microns. This method employs the tracking sensors themselves, with only a minor modifcation to make them highly transparent to infrared light. Only the aluminum metalization on the back of the sensor needs to be swept away in a circular window with a diameter of few millimeters to allow the IR beam to pass through. Since IR light produces a measurable signal in the silicon bulk, there is no need for any extra readout electronics.

A key parameter to understand the ultimate resolution of this method is the transmittance of a silicon sensor and the diffraction of the light. As a first approximation a silicon sensor is viewed as a stack of perfectly homogeneous plano-parallel layers, each characterized by its index of refraction and thickness. The layers are, however, not continuous but present local features, so that diffraction phenomena will appear if the size of the obstacle is comparable to the wavelength used. For instance, the strips of the detector with 50 μm readout pitch, are good examples of an optical diffraction grating for an incoming beam in the IR. It has been determined that a key parameter that determines the overall transmittance of a microstrip detector is the pitch to strip ratio, that is, the fraction of the strip covered by aluminum. The smaller the strip width, the more light is transmitted. It was determined that good transmittance was achieved when the strip width was set to 10% of the pitch.

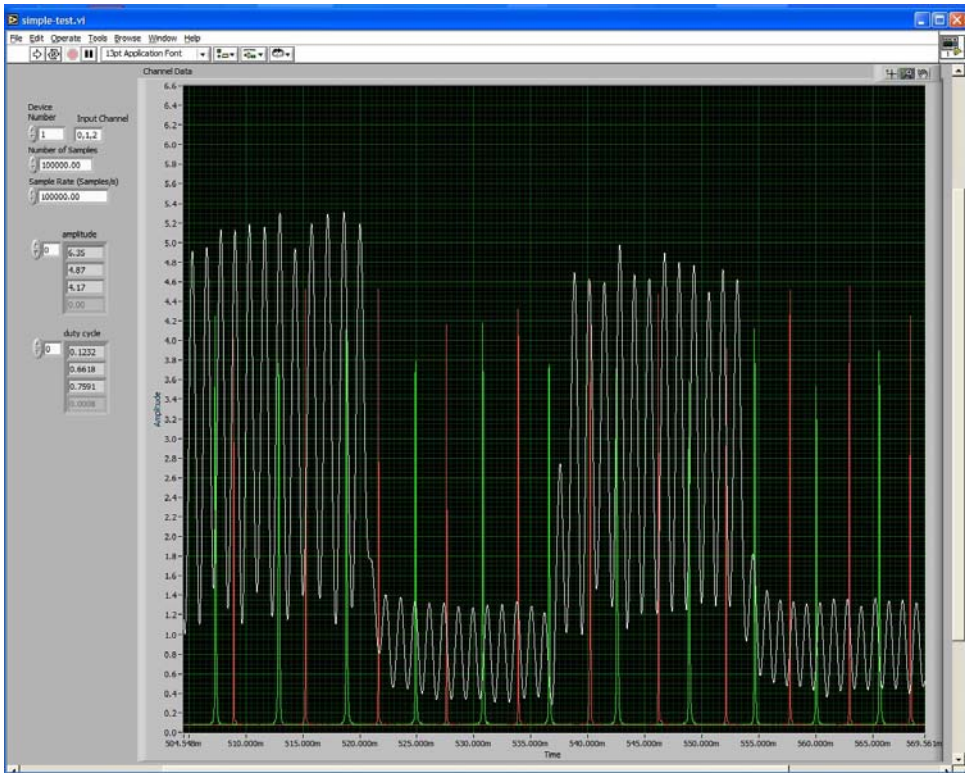

Figure 1.26: Example of FSI fringe display for a single-channel FSI system. White peaks indicate interference fringes, while red and green peaks are Fabry-Perot transmission maxima from a chopped, dual-laser system.

Tuning of sensor thickness was found to contribute up to 5% over the layout optimized value. In bench tests, based on CMS strip detectors, a relative alignment of a few microns has been achieved.

It should be noted that this alignment method has been implemented at the Alpha Magnetic Spectrometer (AMS) and has been by the tracking system of the Compact Muon Solenoid experiment. Furthermore, both methods, developed for central and forward tracker alignment, may also prove useful for the vertex detector.

1.1.12 R&D

1.1.12.1 Sensor Technology

Sensor technology is sensitive to the state of the art in microelectronics. Given the rapid advances in this field, we feel that the choice of vertex detector technology can and should be delayed until either one technology is demonstrated to be superior, or a choice is imposed by the installation schedule for the detector. We note that the detector is physically small and the SiD design allows for installation and service of detector assemblies during shutdowns. The danger with this approach is that it does not allow for early consideration of system

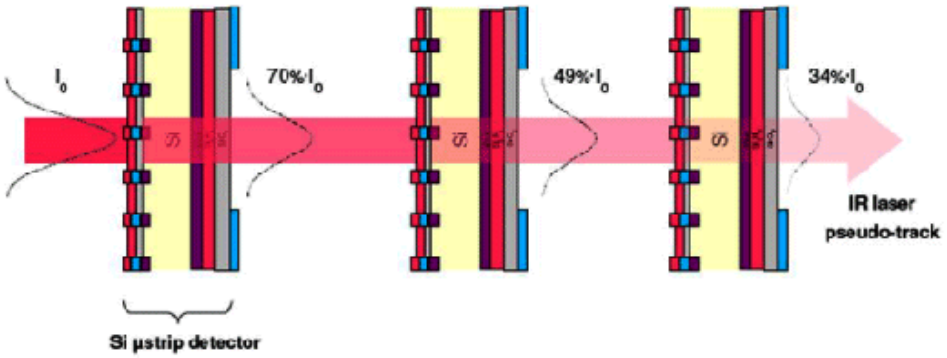

Figure 1.27: Sketch of the IR alignment method.

design aspects that depend on sensor technology. It also requires support of sensor R&D on a rather broad front.

Candidate technologies sensor technologies include:

- CMOS MAPS - Monolithic active pixel sensor where signal charge is produced in the $\approx$ 10 micron thick epitaxial layer available in many standard CMOS processes and collected in an implanted well.
- Charge Coupled Device (CCD) - based technologies
  - ISIS - CCD/CMOS hybrid device where good time resolution and reduction of instantaneous power is achieved by in-pixel storage of multiple CCD raw charge samples.
  - Fine Pixel CCD - CCD with pixel size of about 5 microns. These fine pixels would provide enhanced ability to discriminate MIPS from pairs generated at the IP.
  - Short column CCD - time resolution is achieved by pairing the shared charge in adjacent columns shifted in opposite directions.
- DEPFET - Provides in-pixel storage and amplification of charge using a transistor (DEPFET) integrated on the sensor which serves as both the charge collecting and amplifying node.
- SOI - Uses the substrate in a monolithic Silicon-on-Insulator device as sensor with the

top silicon providing readout electronics. Vias are placed in the buried oxide insulator layer to access the signal charge produced in the bulk silicon "handle".

- 3D - Uses vertical integration of electronics to increase in-pixel functionality and to integrate sensors and ICs. This provides the ability to provide complex electronics and fine pitch pixels without extremely small feature size.

Table 1.6 summarizes some (but not all) of the leading candidate sensor technologies. Some are more easily adapted to fine time resolution which could accommodate smaller detector radii and higher machine backgrounds. Others have advantages for mechanical assembly or power consumption. R&D efforts are focussed on addressing the challenges associated with each technology. We note that the ISIS effort, which provides relatively uniform power dissipation during the inter-train period, has recently been discontinued in the UK.

1.1.12.2 Power

Power distribution and engineering is a crucial part of the vertex design. Air cooling is essential to minimize the mass of the detector. A practical air cooling system limits the heat load in the central barrel to about 20 Watts. This can be achieved in some technologies by pulsing the power applied to the front-end circuitry. Given the 200:1 duty factor of the beam, and assuming that 100:1 can practically be achieved for pulsed powering, this implies a 2,000 Watt peak load for the central barrel. With electronics operating at 1.5 V this implies peak currents of 1333 A. The conductor needed to carry this current with acceptable voltage drop is too massive. To reduce the mass we expect to employ either a serial powering or DC-DC conversion scheme to allow high voltage, low current power delivery.

Work on these technologies has just started.

Fermilab, Penn and RAL have developed the Serial Power Interface (SPi) ASIC, which will enable the testing of pulsed serially powered systems.

The SPi was developed for both SLHC and ILC applications. The chip has two linear and one shunt regulator each with the ability to control the output voltage levels via a control lines, allowing

for a pulsed power mode. We also expect to benefit from work for super-LHC, which will need a high voltage power delivery scheme to keep the size and mass of the

cable plant within acceptable bounds.

Early DC-DC converter prototypes from CMS with air-core inductors show acceptable EMI only when shielded. The mass of these devices is about 0.02 radiation lengths.

The tradeoff between bulkier, higher mass DC-DC systems and serially powered systems which do not naturally have balanced currents and are therefore more susceptible to Lorentz forces needs to be studied. Pulsed powering is unique to ILC, and work to understand the electrical and mechanical impact of power pulsing will be a high priority for most SiD subsystems.

	CMOS MAPS	ISIS CCD	DEPFET	SOI	3D
Advantages	Available technology, moderate in-pixel complexity	EMI resistant, uniform power utilization	Low power, demonstrated functionality	Low noise, large signal, monolithic design	High in-pixel functionality, large S/N, good time resolution
Challenges	Charge collection by diffusion, parasitic collection by PMOS	Time resolution set by in-pixel samples	Limited time resolution, need for auxiliary chips	Back gate effects on transistors limit V_{bias}	Yield of integrated structure
R&D Focus	Complex in-pixel functions, S/N, time resolution	Integration of CMOS and CCD technology	Speed of RS readout, system design	Transistor backgate, commercial availability	Technology demonstration, commercial availability
Readout schemes studied	RS, CP, PS, TS	PS	CP	RS, PS	TS
Form factor	Reticle	Reticle	Full ladder	Reticle	Full ladder
R&D Projects	Mimosa, LDRD, FAPS, CAP, SRD0, Chronopixel	ISIS	DEPFET	LDRD-SOI, CAP5	VIP1,2

Table 1.6: Summary of the characteristics of some candidate vertex sensor technologies. In the Readout Scheme row RS=Rolling Shutter, CP=Column Parallel, PS=Pipelined Storage, TS=Time Stamp.

1.1.12.3 Outer Tracker

The ILC experiments demand tracking systems unlike any previously envisioned. In addition to efficient and robust track-finding over the full solid angle, the momentum resolution required to enable precision physics at ILC energies must improve significantly beyond that of previous trackers. The design must minimize material in front of the calorimeter that might compromise particle-flow jet reconstruction. Establishing and maintaining the alignment for the tracker is critical. Even with the largest feasible magnetic field, the tracking volume is quite large, demanding optimized tracker components which facilitate mass production. Finally, the tracker must be robust against beam-related accidents and aging. All these requirements must be maintained within a "push-pull" scenario.

The emphasis in the area of the tracking detector is currently on the development of the double-metal sensor with the associated readout. These sensors need to work in a 5 T magnetic field and remain stable and aligned during power pulsing. The forward tracker design must be optimized. A small scale system consisting of a few sensors with full readout will be tested in a test beam under these operating conditions. Only then can issues associated with the Lorentz forces and mechanical stability be tested.